Evidence from central Mexico supporting the Younger Dryas extraterrestrial impact hypothesis

Isabel Israde-Alcántara[a], James L. Bischoff[b,1], Gabriela Domínguez-Vázquez[c], Hong-Chun Li[d], Paul S. DeCarli[e], Ted E. Bunch[f], James H. Wittke[f], James C. Weaver[g], Richard B. Firestone[h], Allen West[i], James P. Kennett[j], Chris Mercer[k], Sujing Xie[l], Eric K. Richman[m], Charles R. Kinzie[n], and Wendy S. Wolbach[n]

[a]Departamento de Geología y Mineralogía, Edif. U-4. Instituto de Investigaciones Metalúrgicas, Universidad Michoacana de San Nicólas de Hidalgo, C. P. 58060, Morelia, Michoacán, México; [b]US Geological Survey, Menlo Park, CA, 94025; [c]Facultad de Biología, Universidad Michoacana de San Nicólas Hidalgo C. P. 58060, Morelia, Michoacán, México; [d]Department of Geosciences, National Taiwan University, Taipei 106, Taiwan, Republic of China; [e]SRI International, Menlo Park, CA 94025; [f]Geology Program, School of Earth Science and Environmental Sustainability, Northern Arizona University, Flagstaff AZ 86011; [g]Wyss Institute for Biologically Inspired Engineering, Harvard University, Cambridge, MA 02138; [h]Lawrence Berkeley National Laboratory, Berkeley, CA 94720; [i]GeoScience Consulting, Dewey, AZ 86327; [j]Department of Earth Science and Marine Science Institute, University of California, Santa Barbara, CA 93106; [k]National Institute for Materials Science, 1-2-1 Sengen, Tsukuba, Ibaraki, 305-0047, Japan; [l]CAMCOR High Resolution and MicroAnalytical Facilities, University of Oregon, Eugene, OR 97403; [m]Materials Science Institute, University of Oregon, Eugene, Oregon 97403; and [n]Department of Chemistry, DePaul University, Chicago, IL 60614

We report the discovery in Lake Cuitzeo in central Mexico of a black, carbon-rich, lacustrine layer, containing nanodiamonds, microspherules, and other unusual materials that date to the early Younger Dryas and are interpreted to result from an extraterrestrial impact. These proxies were found in a 27-m-long core as part of an interdisciplinary effort to extract a paleoclimate record back through the previous interglacial. Our attention focused early on an anomalous, 10-cm-thick, carbon-rich layer at a depth of 2.8 m that dates to 12.9 ka and coincides with a suite of anomalous coeval environmental and biotic changes independently recognized in other regional lake sequences. Collectively, these changes have produced the most distinctive boundary layer in the late Quaternary record. This layer contains a diverse, abundant assemblage of impact-related markers, including nanodiamonds, carbon spherules, and magnetic spherules with rapid melting/quenching textures, all reaching synchronous peaks immediately beneath a layer containing the largest peak of charcoal in the core. Analyses by multiple methods demonstrate the presence of three allotropes of nanodiamond: n-diamond, i-carbon, and hexagonal nanodiamond (lonsdaleite), in order of estimated relative abundance. This nanodiamond-rich layer is consistent with the Younger Dryas boundary layer found at numerous sites across North America, Greenland, and Western Europe. We have examined multiple hypotheses to account for these observations and find the evidence cannot be explained by any known terrestrial mechanism. It is, however, consistent with the Younger Dryas boundary impact hypothesis postulating a major extraterrestrial impact involving multiple airburst(s) and and/or ground impact(s) at 12.9 ka.

black mat | cosmic impact

We present data from Lake Cuitzeo in central Mexico (19.94 °N, 101.14 °W) in support of evidence for the Younger Dryas (YD) impact hypothesis, as first presented at the 2007 Meeting of the American Geophysical Union in Acapulco, Mexico. There, a consortium of scientists reported geochemical and mineralogical evidence from multiple terrestrial sites ascribed to extraterrestrial (ET) impacts and/or airbursts (1). Their first evidence was the discovery at well-dated Clovis-era archeological sites in North America of abundant magnetic spherules (MSp) and carbon spherules (CSp) in a thin layer (0.5 to 5 cm) called the Younger Dryas boundary layer (YDB), dating to 12.9 ± 0.1 ka BP (calibrated, or calendar years) or 10.9 ^{14}C ka BP (radiocarbon years)[†] (1–3). The YDB is commonly located directly beneath or at the base of an organic-rich layer, or "black mat," broadly distributed across North America (1). Later, abundant nanodiamonds (NDs) were discovered by Kennett et al. (2, 3) in the YDB layer at numerous locations. NDs also were detected at the margin of

the Greenland Ice Sheet in a layer that dates to the approximate YD onset (4). These discoveries led to the hypothesis that one or more fragments of a comet or asteroid impacted the Laurentide Ice Sheet and/or created atmospheric airbursts (1) that initiated the abrupt YD cooling at 12.9 ka, caused widespread biomass burning, and contributed to the extinction of Late Pleistocene megafauna and to major declines in human populations (5).

Some independent workers have been unable to reproduce earlier YDB results for MSp, CSp, and NDs (6–8), as summarized in a "News Focus" piece in *Science* (9), which claims that the YDB evidence is "not reproducible" by independent researchers. Refuting this view, multiple groups have confirmed the presence of abundant YDB markers, although sometimes proposing alternate hypotheses for their origin. For example, Mahaney et al. (10–12) independently identified glassy spherules, CSps, high-temperature melt-rocks, shocked quartz, and a YDB black mat analogue in the Venezuelan Andes. Those authors conclude the cause was "either an asteroid or comet event that reached far into South America" at 12.9 ka. At Murray Springs, Arizona, Haynes et al. (13) observed highly elevated concentrations of YDB MSp and iridium. Abundances of MSp were 340 × higher than reported by Firestone et al. (1) and iridium was 34 × higher, an extraordinary enrichment of 3,000 × crustal abundance. Those authors stated that their findings are "consistent with their (Firestone et al.'s) data." In YDB sediments from North America and Europe, Andronikov et al. (2011) reported anomalous enrichments in rare earth elements (REE) and "overall higher concentrations of both Os and Ir [osmium and iridium]" that could "support the hypothesis that an impact occurred shortly before the beginning of the YD cooling 12.9 ka."[‡] Tian et al. (14)

observed abundant cubic NDs at Lommel, Belgium, and concluded that "our findings confirm … the existence of diamond nanoparticles also in this European YDB layer." The NDs occur within the same layer in which Firestone et al. (1) found impact-related materials. Similarly, at a YDB site in the Netherlands, Van Hoesel et al.[§]observed "carbon aggregates [consistent with] nanodiamond." Recently, Higgins et al.[¶] independently announced a 4- to 4.5-km-wide YDB candidate crater named Corossol in the Gulf of St. Lawrence, containing basal sedimentary fill dating to 12.9 ka. If confirmed, it will be the largest known crater in North and South America within the last 35 million years

Because of the controversial nature of the YD impact debate, we have examined a diverse assemblage of YDB markers at Lake Cuitzeo using a more comprehensive array of analytical techniques than in previous investigations. In addition, different researchers at multiple institutions confirmed the key results.
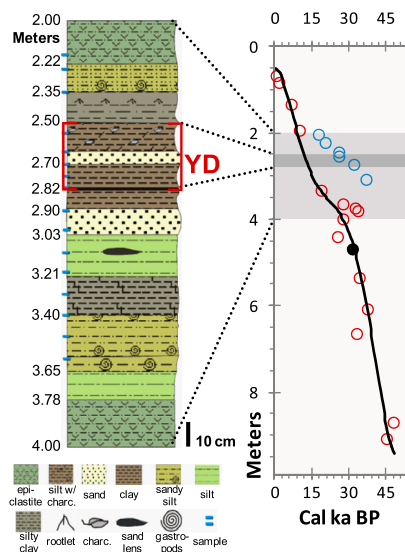
Lake Cuitzeo

Covering 300–400 km^2, Cuitzeo is the second largest lake in Mexico, located at high elevation of 1,820 m in the northern part of the state of Michoacán within the tectonically active Trans Mexico volcanic arc (15) (*SI Appendix*, Fig. 1). Situated in the tropics, this lake currently experiences a semiarid climate with annual temperatures ranging from 10 to 28 °C (avg 19 °C) and annual rainfall ranging from 60 to 100 cm. This shallow lake currently varies in depth from 0.8 to 2.2 m (avg 1.9 m).

Results

Sedimentary Sequence. A 27-m-long, 10-cm-diameter core was extracted in 1997 from thick deposits in Lake Cuitzeo as part of an interdisciplinary, multiproxy effort to acquire a detailed paleoclimate record extending back to the last interglacial [130,000 (130 kyr)] (15). The core consists of interbedded sands, silts, clays, and epiclastites, along with 6-kyr-old, 20-cm-thick tephra between 1.7 and 1.4 m and 31.5-kyr-old, 20-cm-thick tephra between 4.7 and 4.5 m, with several more volcanic deposits below 10 m. A conspicuous, dark, carbon-rich layer, dominantly comprised of clay and silt, occurs between 2.82 and 2.50 m (Fig. 1) and is the focus of this study because of its similarity to the black mat at YDB sites across North America. Sediment samples of approximately 1 cm thickness were taken every 5 cm across the critical section between 2.80 and 2.65 m and at 10 cm intervals above and below this section. These samples were quantitatively analyzed for diatoms and pollen assemblages, carbonate (%TIC), organic carbon (% TOC), bulk major-element composition, stable carbon isotopes (both organic and inorganic), organic nitrogen, MSp, NDs, CSp, charcoal, and aciniform soot.

Chronology. Previously, Israde et al. (15) published an age-depth model for the uppermost 9 m at Lake Cuitzeo comprised of 16 accelerator mass spectroscopy (AMS) ^{14}C dates on bulk sediment and used in a linear interpolation with the YD onset identified at approximately 2.8 m. To test and refine that model, we acquired six more AMS ^{14}C dates on bulk sediment, for a total of 22 dates, and calibrated them using the IntCal04 calibration curves in CalPal07[‖] (Fig. 1; *SI Appendix*, Table 1). A 20-cm-thick tephra layer at 4.7 to 4.5 m has been identified as the Cieneguillas rhyolitic tephra, originating from nearby Las Azufres volcano and ^{14}C dated by others at three locations to approximately 31 ka (26.8 ± 0.9 ^{14}C ka) (16). The age of this tephra serves as an anchor for the chronology. The dates from 9 to 3.35 m and from

Fig. 1. (*Left*). Lake Cuitzeo lithostratigraphy from 4.0 to 2.0 m. Red brackets indicate the carbon-rich layer corresponding to the YD. Blue tick marks at left indicate sample depths. (*Right*) Graph of calibrated ^{14}C dates. A regression polynomial (black line) of accepted dates (red circles) and tephra date (black dot); blue circles are excluded dates. Error bars are less than circle widths. Dark gray band denotes YD interval; lighter gray band corresponds to interval between 4.0 and 2.0 m. Cal ka BP, calibrated kiloannum before present; char, charcoal.

2 to 0 m show a relatively consistent linear increase with depth, ranging in age from approximately 46 to 0 kyr.

The samples at 3.35 and 1.95 m have calibrated ages of 18.8 and 9.9 ka, respectively, consistent with the linear extrapolation of the rest of the core. However, six samples between these two levels provided radiocarbon ages older than the interpolation predicts. They represent a major radiocarbon reversal of thousands of years, with older sediment overlying younger, a situation that can result from reworking of older organic material. The reversal begins with a date of 18.8 ka above, shifts anomalously older by approximately 20 kyr above, and then normalizes to 9.9 ka higher in the section. At 2.75 m within this interval, total organic carbon (TOC) is 15.8 wt%, the highest percentage in approximately 100 kyr (15). This sample yields a date of approximately 32 ka, but linear interpolation indicates it should date to approximately 13 ka, a difference of approximately 20 kyr. Accounting for this shift requires major contamination of the TOC by radiocarbon-dead or very old carbon (92 wt%). Currently, the source of this old carbon remains unclear.

To compensate for these anomalously old radiocarbon dates, we excluded the six dates that form the reversal between 3.10 and 2.05 m and utilized the remaining 16 dates to generate an age-depth curve with a fifth-order polynomial regression[**]. The resulting curve (Fig. 1), predicts that the 12.9-ka YD onset is at a depth of approximately 2.9 to 2.7 m, consistent with the earlier identification by Israde et al. (15).

Biostratigraphy. Although the stratigraphic position of the YD onset has been reasonably extrapolated using numerous ^{14}C dates, as is standard practice, we have examined other stratigraphic data to assist with this placement of the YD onset. This is achieved using biostratigraphic correlation of pollen sequences from Lake Cuitzeo with those from YD-aged regional lakes that have been independently dated. Islebe and Hooghiemstra (17) reported that evidence for YD climate change is either present or likely in some, but not all, lakes in Mexico, Guatemala, Costa Rica, Colombia, Ecuador, and Peru. Of those mentioned, we have

---

[§]Van Hoesel A, Hoek W, Braadbaart F, van der Plicht H, Drury MR, Nanodiamonds and the Usselo layer, INQUA XVIII, July 21–27, 2011, Bern Switzerland, #1556.

[¶]Higgins MD, et al., Bathymetric and petrological evidence for a young (Pleistocene?) 4-km diameter impact crater in the Gulf of Saint Lawrence, Canada, 42nd Lunar and Planetary Science Conference, March 7–11, 2011, The Woodlands, TX, 1504 LPI Contribution No. 1608.

[‖]http://www.calpal.de

[**]$y = -5E{-}07x^5 + 6E{-}05x^4 - 0.0025x^3 + 0.0366x^2 - 0.0108x + 0.512$; $R^2 = 0.946$

examined pollen records from Lake Petén Itzá in Guatemala (18, 19), La Chonta Bog in Costa Rica (20), and Lake La Yeguada in Panama (21) (*SI Appendix*, Fig. 2). The pollen sequences from these lakes reflect climate changes, including the Late Glacial, Bølling–Allerød (BA), (14.5 to 12.9 ka), YD stadial (12.9 to 11.5 ka), and the Holocene (11.5 ka to present), comprising a distinctive cold-warm-cooler-warmer climatic sequence. The YD interval was specifically identified by previous investigators at Lakes La Chonta and Petén Itzá.

Pollen changes in Lake Petén Itzá at the YD onset display a decrease in *Quercus* (oak), a persistence of *Pinus* (pine), a dominance of Poaceae (grasses), and low diversity and productivity for plants in general (19). At or near the YD onset, the record at Petén Itzá exhibits exceedingly large, abrupt, and unprecedented changes (both in magnitude and rate of change) for temperature, rainfall, and biotic turnover. These changes produced the most distinctive layer in the Late Quaternary record (18, 19).

For Lake La Yeguada, although the YD episode was not expressly identified, workers there recognized a major, abrupt environmental and ecological change (a "time of crisis") close to the onset of the YD at approximately 12.8 ka (10.8 ^{14}C ka) (20). This is reflected in dramatic changes in the pollen and diatom records, biotic turnover, clay mineralogy, sedimentary geochemistry, and particulate carbon flux. At the same time, *Quercus* and *Myrtaceae* (myrtle) were replaced by Poaceae. These changes represent the most distinctive layer in this record (21).

In these regional lakes, the pollen records typically form a "peak-trough-peak" pollen pattern with the trough representing very low pollen levels during the YD (Fig. 2; *SI Appendix*, Table 2). At Cuitzeo, total pollen and *Quercus* reveal a similar pattern in which high pollen abundances below 2.9 m correspond to the BA when warmer temperatures supported abundant biota around the lake. Low pollen abundances in the trough correspond to the YD interval. For all lakes, the unique, distinctive BA pollen peaks are among the largest in the last 40 to 100 kyr and are followed during the YD by some of the lowest total pollen values, consistent with a cooler and/or drier climate. After the YD, a rebound of varying magnitude occurred at all lakes after the Holocene began at 11.5 ka.

Because climate change also affects diatom populations, we compared the diatom record at Cuitzeo with other lakes, and as with pollen, the diatom record reveals a period of extraordinary change at the YD onset. *Stephanodiscus niagarae* and *Aulacoseira spp*. display major YD abundance peaks that are among the largest in the last 100 kyr (*SI Appendix*, Fig. 3 and *Biostratigraphy*). For Cuitzeo diatom assemblages, we also plotted the change in diversity ("δ diversity"), defined as the value derived from subtracting the total number of diatom species in one sample from the adjacent sample above it. This demonstrates that the greatest change in diversity within >50 kyr occurred at the YD onset at 2.8 m in Lake Cuitzeo (δ diversity in *SI Appendix*, Fig. 3), and this correlates well with the Lake La Yeguada record where the greatest turnover in diatom species occurred at approximately 12.8 ka (10.8 ^{14}C ka) (21). In addition, for Lakes Cuitzeo and La Yegua-

da, especially large YD peaks are evident in other aquatic taxa, including cattails *(Typha)* and the algal forms *Botryococcus* and *Coelastrum* (*SI Appendix*, Fig. 4). High abundances for these taxa are consistent with major ecological change at the YD onset.

In Fig. 2, we compare the pollen records to a temperature proxy (δ^{18}O) from a Greenland ice core, GISP2 (22). We have also correlated paleoceanographic records from the Cariaco Basin in the Caribbean (Fig. 2), in which titanium represents terrigenous input due to continental runoff (23) and molybdenum varies in response to deglacial climate change (24). The YD onset is identified in all three records and corresponds well with the pollen records from Cuitzeo and other lakes.

In summary, from widely separated lakes in the highlands of Costa Rica to the lowlands of Guatemala and Panama, there is only one stratigraphic interval that displays extraordinary environmental and biotic changes, and in each case, this interval occurs at or near the YD onset. For Lake Cuitzeo, the age-depth model indicates the YD onset occurs between 1.95 and 3.35 m, representing a 9-kyr span. Within this span, only one level displays extraordinary environmental and biotic changes, as in other regional lakes, and that level is at 2.8 m. Therefore, we conclude that the Cuitzeo age-depth model is robust and that the YD onset is correctly identified at 2.8 m.

Sedimentary Geochemistry. Our attention was first drawn to the anomalous interval of unusually high values of TOC (5–16%) occurring between 4.0 and 2.6 m, particularly a TOC of 15.8% in the thin, 1-cm-thick layer at 2.75 m, close to the YD onset (Fig. 3). This value is the highest TOC in the entire 27-m core, which has a background average of only 1.2%. We performed δ^{13}C analyses, and below 2.75 m, there are minor fluctuations near an average of −2‰, which is typical for algal matter. Above 2.75 m, δ^{13}C values increase 10 × to −19‰ at 2.7 m in the dark layer, followed by heavier values above 2.0 m (after approximately 10 ka) in the Holocene. The 2.75-m layer is depleted in phosphorus, producing a distinct carbon/phosphorus ratio (C/P) peak that is the highest in core. This material may be analogous to the YD carbon-rich black mat observed at many North American sites (25). When viewed with the scanning electron microscope (SEM), the 2.75-m layer contains thin millimeter-sized interbeds of black organic carbon that appear without form or structure. Analysis by energy-dispersive X-ray spectroscopy (EDS) indicates these bands are almost pure elemental carbon.

Organic matter in the anomalous interval is enigmatic and not the normal plant-derived kerogenous organic matter, dominating the rest of the 27-m core over the last 100 kyr; instead, it appears to be very old and radiocarbon-dead. Pyrolysis analysis (Rock/Eval) was conducted on samples from the carbon-rich layer between 2.90 and 2.55 m and then compared with a carbon-rich sample from the YD-aged black mat at Murray Springs, Arizona (*SI Appendix*, Table 3), as previously analyzed by Bischoff in Haynes (25). This comparison suggests that much of the TOC is unreactive carbon, whereas, according to GC-MS analysis, the remaining extractable carbon fraction is typical of immature
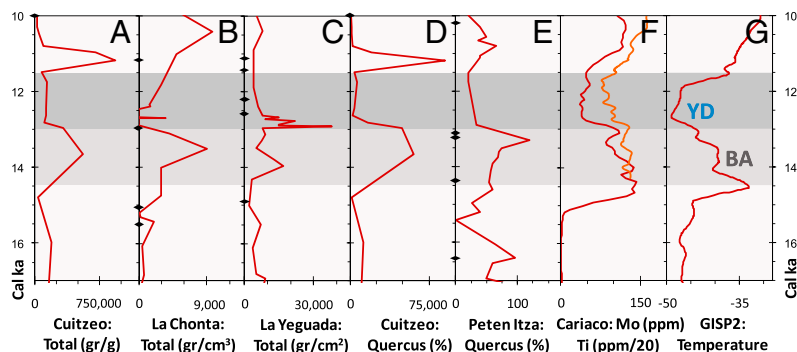
Fig. 2. Graphs for pollen, Cariaco Basin proxies, and GISP2 temperatures. (*A*–*C*) compare Lake Cuitzeo pollen abundances to two regional lakes. Warmer Bølling–Allerød (BA) in light gray, and YD in dark gray. *D* and *E* show that Lake Cuitzeo *Quercus* abundances are similar to those of Lake Petén Itzá. All lake plots correspond well to graph *F* from a Cariaco Basin core displaying ppm abundances of titanium (orange; smoothed 30 ×) and molybdenum (red; smoothed 3 ×) (23, 24). Graph *G* is a GISP2 temperature proxy plot (‰ δ^{18}O; smoothed 10 ×) (22). Black diamonds are depth of ^{14}C dates. All graphs are similar, demonstrating that the YD onset is consistent at all sites.
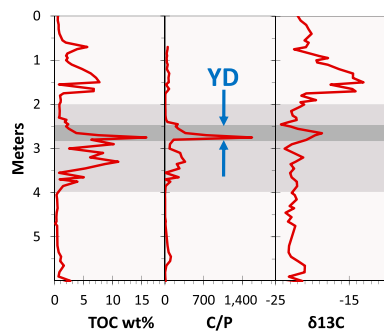
Fig. 3. Changes in carbon for the upper 6 m of the Lake Cuitzeo sequence. There YD onset peaks in TOC wt%, C/P, and δ^{13}C. The dark gray band denotes the YD interval, and the light gray band is the interval between 4.0 and 2.0 m.

plant-derived compounds, mostly n-alkanes. Contamination of carbon from petroleum seeps, such as those in Lake Chapala 300 km to the west, was explored as a possible source of the anomalous carbon (26). However, pyrolysis analysis showed no detectable petroleum hydrocarbons in the sequence analyzed. This carbon does not appear to be derived from typical immature plant compounds, and its origin is unknown.

Impact Proxies

CSp, Charcoal, and Aciniform Soot. Black CSp, 20 to 260 μm, averaging 90 μm diameter, were observed at Cuitzeo, appearing as ovoid-to-round with cracked, roughened surfaces and typically revealing a thin rind, with spongy, vesicular interiors surrounded by a smooth, homogeneous matrix (*SI Appendix,* Fig. 5). SEM-EDS indicates that CSp are dominantly carbon (>87%) with minor particulates, such as Si, Al, and Fe, concentrated in the rind. They reach a significant peak of approximately 680/kg at 2.75 m within the YDB layer. Above 2.75 m, the CSp persist at an average of approximately 120/kg. No CSp were detected below 2.8 m.

Charcoal microparticles (>125 μm) were counted between 3.6 and 2.2 m, an interval dating from approximately 21 to 10 ka (Fig. 4), displaying background levels of approximately 5,000 particles/kg. There is a minor charcoal peak at 3.1 m of approximately 29,000 particles/kg, dating to approximately 16 ka, and there is a major rise in charcoal beginning near the YD onset and reaching a maximum peak at 2.65 m of 77,000 particles/kg (15 × background) in a major episode in biomass burning. The main charcoal peak is about 5 cm above the impact proxies discussed below, and the lack of tephra within this interval indicates the biomass burning is unrelated to volcanism. There is also a major peak in particulate carbon (charcoal) in Lake Le Yeguada that dates close to 12.8 ka (21), near the YD onset.
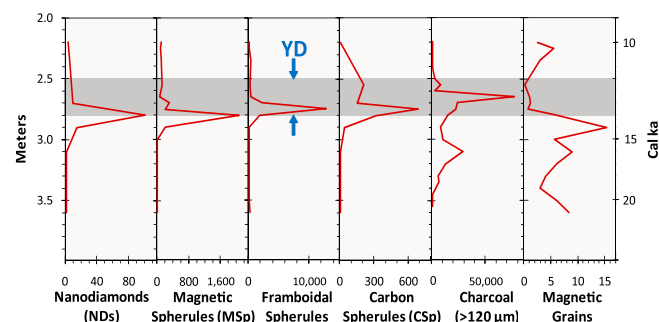
Fig. 4. Markers over the interval between 3.6 and 2.2 m. The YD episode (12.9 to 11.5 ka) is represented by dark band. YDB layer is at 2.8 m. NDs and magnetic impact spherules both peak at the YD onset, whereas framboidal spherules, CSps, and charcoal peak higher in the sequence. Magnetic grains peak just prior to the YD onset. NDs are in ppb; Msps, framboidal spherules, CSps, and charcoal are in no./kg; magnetic grains in g/kg.
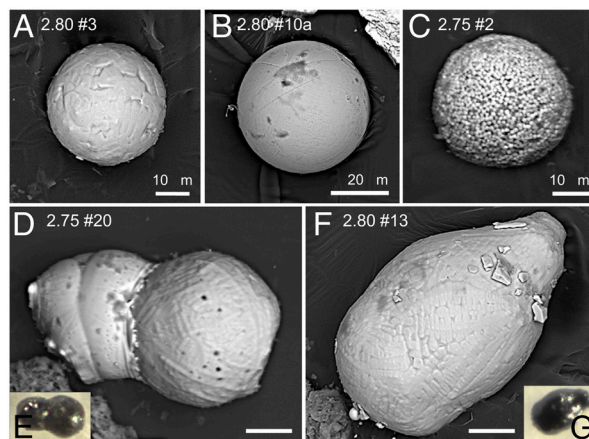
Fig. 5. SEM images of magnetic impact spherules. (*A–B*) Magnetic impact spherules with dendritic surface pattern. (*C*) Framboidal pyrite spherule. (*D*) Collisional magnetic impact spherules. (*E*) Light micrograph of same magnetic impact spherules. (*F*) Teardrop-shaped spherule with dendritic pattern. (*G*) Photomicrograph of same MSps. For labels such as "2.80 #3," "2.80" represents depth of sample in meters and "#3" is the magnetic impact spherule number as listed in *SI Appendix,* Table 4.

MSp and Particles. All samples from Cuitzeo contain a variable mix of MSp, magnetic grains, framboidal spherules, and/or weakly magnetic volcanic glass (Fig. 4; *SI Appendix,* Tables 4 and 5). MSp range from 25–100 μm in diameter, averaging 60 μm (Fig. 5), and typically appear as highly reflective, black spheroids (Fig. 5 *A* and *B*; *SI Appendix,* Fig. 6 *B* and *E*), although shapes such as ovals, doublets, dumbbells, and tear-drops frequently occur (Fig. 5 *D–G*; *SI Appendix,* Fig. 6 *A, C, and D*). The MSp are conspicuous and abundant at 2.8 m (2,000/kg), where they form a sharp peak in the YDB. They average approximately 100 MSp/kg above the YDB, and none were detected at depths of 3.6 to 3.0 m.

SEM observation of outer surfaces of all MSp analyzed reveals a surficial crystalline pattern that is dendritic (Fig. 5 *D* and *F*) or polygonal like a soccer-ball (Fig. 5*A*; *SI Appendix,* Fig. 6*E*). These patterns are indicative of melting with rapid quenching[††], which precludes diagenetic, biogenic, or detrital origins. Several MSp clearly display evidence of interspherule collisions while solidifying, causing fusion (Fig. 5 *D* and *E*). EDS analyses of the recovered MSp show that they are comprised of magnetite (Fe oxide >96%) with very low abundances of other elements (*SI Appendix,* Table 4). Because titanium is present at only trace levels in the MSp, they are not titanomagnetite grains, which are ubiquitous throughout the Cuitzeo core.

We observed variable abundances of irregularly shaped titanomagnetite grains throughout the sequence, peaking well below the YD onset (Fig. 4). Typically black and moderately reflective, these grains are monocrystalline and geochemically distinct from MSp and are interpreted to be detrital material from the local volcanic regolith. Pinter et al. (27) speculated that all previously reported YDB MSp are actually detrital grains or framboidal spherules, but this is refuted at Lake Cuitzeo because such grains are readily distinguishable from YDB MSp by the quench-melted textures visible by SEM imaging.

Irregularly shaped volcanic glass grains (<1 μm to several mm long) occur in all layers and contain up to 10% Fe causing them to be magnetic. They were observed in relatively uniform abundances throughout the section, uncorrelated with the MSp peak. Most appear dark-gray to black, translucent-to-opaque, and are highly reflective. SEM imaging revealed vesicles (gas bubbles)

[††]Petaev MI, Jacobsen SB, Basu AR, Becker L, Magnetic Fe, Si, Al-rich impact spherules from the P-T boundary layer at Graphite Peak, Antarctica, 35th Lunar and Planetary Conference, March 15–19, 2004, Houston, TX, 1216 (abstr.).

that formed in the glass as it cooled. Using a standard igneous rock binary diagram, the glass grains are identified as alkali basalt, andesite, rhyolite, rhyodacite, tephrite, and latite (trachyandesite) (*SI Appendix*, Fig. 7). These glass grains are considered to be of local volcanic origin. In contrast, none of the quenched MSp plotted on the graph, indicating a different origin.

Framboidal spherules (approximately 20 to 60 μm, averaging approximately 40 μm in diameter) are concentrations of euhedral microcrystals typical of diagenetic sedimentary pyrite (28) (Fig. 5C; *SI Appendix*, Fig. 6F). Framboidal spherules were found intermixed with MSp, forming a distinct abundance peak in the YDB layer at 2.75 m, where they occur at 10,000/kg (Fig. 4). None were detected below the base of the YDB at 2.80 m. On the other hand, above 2.75 m, framboidal spherules were relatively common, averaging a few hundred per kg. The origin of the framboidal spherules is unclear, but their formation most likely resulted from the onset of anoxic conditions beginning near 12.9 ka.

We have compared and contrasted the geochemistry of MSp, framboidal spherules, glassy grains, and magnetic grains from the Cuitzeo YDB layer using SEM-EDS. A ternary diagram in Fig. 6A compares FeO, SiO$_2$, and TiO$_2$ and demonstrates that the MSp are geochemically dissimilar to volcanogenic material. Next, the geochemistry of the YDB MSp was plotted on ternary diagrams and compared to that of other types of spherules and melted material. In Fig 6B, no similarity was observed when compared with particles representative of cosmic influx and meteoritic ablation, including >700 meteorites and cosmic spherules (*SI Appendix*, Table 6). Instead, geochemical values for Cuitzeo MSp are similar to those for >1,000 tektites (glassy, melted impact material) and MSp from 11 craters/strewnfields formed by ET impact into terrestrial rocks (Fig 6C; *SI Appendix*, Table 6), suggesting that Cuitzeo MSp also formed by cosmic impact.

NDs. A definitive proxy for the YD impact event is an abundant and diverse assemblage of NDs within the YDB layer across North America (2, 3) and in the Greenland Ice Sheet (4). Four allotropes of NDs have been previously identified, including cubic NDs and lonsdaleite, which has only been found on Earth associated with impact craters or within meteoritic material (29–31).The other two allotropes, n-diamond and i-carbon, were first discovered in the laboratory and are considered to be either diamond-like carbon or modified cubic NDs (32, 33).

In a comprehensive investigation of NDs at Cuitzeo, we selected eight bulk samples spanning 1.4 m from 3.6 to 2.2 m that included the YD interval within an age range from 21 to 10 ka. Noncontinuous approximate 1-cm-thick samples, ranging from approximately 4 to 23 g (approximately 3 to 20 cm^3) were taken at intervals of 5 cm across the inferred YDB and at intervals of 10 to 50 cm away from the YDB. Using procedures described in Kennett et al. (2, 3), we produced acid-resistant residue for each bulk sample to concentrate any NDs (*Methods*; *SI Appendix*, *Methods*). In response to a challenge by Daulton et al. (8) that

the YDB contains no NDs, we examined these residues using a highly comprehensive suite of analyses surpassing previous investigations. Analyses were conducted on high-resolution transmission electron microscopes (HRTEM) and scanning transmission electron microscopes (STEM), discussed below.

These analyses clearly identified a single major peak in NDs, centered across two samples at 2.8 and 2.75 m within the dark layer dating to the YD onset. NDs were rare below the 2.9 m layer [≤1 parts per billion (ppb)], whereas above the 2.75 m layer, NDs were observed at low levels from 4 to 10 ppb, likely due to reworking. Initial examination of the 2.8 m sample using STEM and HRTEM revealed a striking panorama of tens of thousands of nanocrystalline carbon particles ranging in shape from spherical to elongate to euhedral (*SI Appendix*, Fig. 8). These particles varied in diameter from approximately 1 to 10 nm, averaging approximately 4 nm, and were typically embedded in amorphous carbon, as Tian et al. (14) described. We identified three of four previously reported ND variants, of which n-diamond was most abundant, with lesser amounts of i-carbon and lonsdaleite. The presence and concentrations of cubic NDs are unclear, for reasons discussed below. The NDs exhibit maximum abundance at 2.8 m of approximately 100 ± 50 ppb (*SI Appendix*, Table 5), similar to the estimates for YDB NDs across North America and Greenland (2–4).

EDS analyses of five samples indicate that the observed crystals are dominantly carbon (averaging 96 atomic %) with minor concentrations of other elements (*SI Appendix*, Table 7). Using noncopper grids (gold and molybdenum) for all five EDS analyses, we detected no copper, refuting speculation by Daulton et al. (8) that YDB NDs are comprised of copper and not carbon.

Selected area diffraction (SAD) was used to identify the dominant types of carbon crystals present in the samples. Many analyses revealed ring diffraction patterns with d-spacings that are consistent with n-diamond (Fig. 7A; *SI Appendix*, Table 8), with a face-centered cubic structure with space group Fm3m (34). Other SADs indicated d-spacings characteristic of i-carbon (35) (Fig. 7B; *SI Appendix*, Table 8), a primitive cubic crystalline structure with space group $P2_13$ or $P4_232$ (32). Crystals with d-spacings consistent with cubic nanodiamond were also observed, but identification was not conclusive.

Fast Fourier transform (FFT) is an analytical procedure that produces diffraction patterns for small single crystals. HRTEM and FFT images of the nanocrystals reveal lattices and d-spacings that are consistent with lonsdaleite, space group $P6_3/mmc$ (Fig. 8 A and B; *SI Appendix*, Table 8) and with n-diamond, space group Fm3m (Fig. 8 C and D).

Electron energy loss spectroscopy (EELS) was utilized to confirm that the observed nanoparticles are carbon and crystalline, as previously indicated by HRTEM, FFT, and SAD analyses. EELS spectra further indicate that the nanoparticles display sp^3 and sp^2 bonding consistent with n-diamonds and i-carbon. Independent published spectra of NDs are plotted for comparison with those
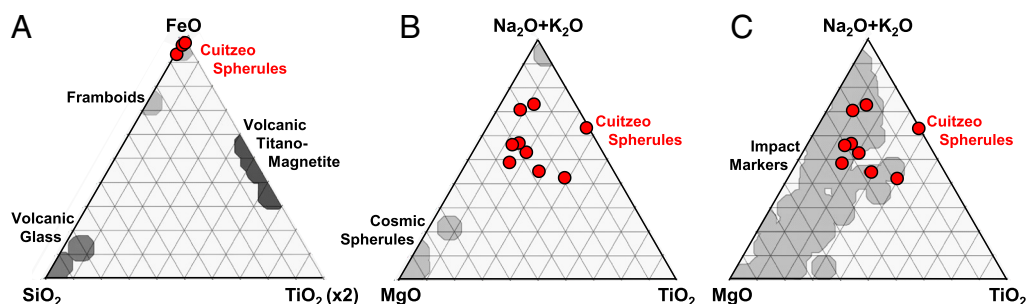
Fig. 6. Ternary geochemical diagrams: (*A*) Cuitzeo magnetic impact spherules compared to volcanogenic titanomagnetite and glassy grains, as well as framboidal spherules. Cuitzeo magnetic impact spherules are nonvolcanogenic. Of two framboidal spherules analyzed, one overlaps the magnetic impact spherules and one does not. Neither exhibits quench melting. (*B*) Cosmic particles compared to Lake Cuitzeo magnetic impact spherules, indicating they are noncosmic. (*C*) Terrestrial impact materials compared to Lake Cuitzeo magnetic impact spherules, showing close geochemical match.

Israde-Alcántara et al.
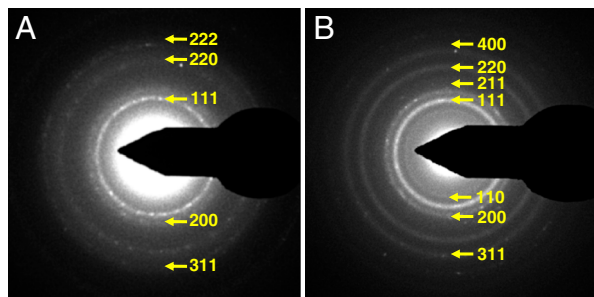
Fig. 7. SAD patterns of NDs from 2.7 m. (*A*) D-spacings indicative of n-diamonds. (*B*) D-spacings indicative of i-carbon.

for Cuitzeo NDs in Fig. 9 (4, 32, 34, 36, 37). The small prepeak at approximately 284 eV indicates sp^2 bonding and is similar for all curves. This prepeak has been previously interpreted by others to result from a graphitic or amorphous coating on the NDs (*SI Appendix, EELS Analyses*). The spectrum does not permit definitive identification of the other two allotropes, cubic NDs, and lonsdaleite. Another EELS spectrum confirmed a lack of copper in the analyzed particles (*SI Appendix,* Fig. 9).

Energy-filtered TEM analysis (EFTEM), an EELS-related mapping technique, was used to investigate the elemental composition of the nanocrystals. We produced two maps of a region of nanoparticles by searching for specific energy levels indicative of carbon. First, a "zero-loss" image (Fig. 10*A*) was acquired and inverted to negative for easier comparison. It displays brighter particles (numbers 1 through 4) that were embedded in amorphous carbon, but exhibit a crystalline structure. Second, a "jump ratio" image (Fig. 10*B*) shows the same particles (numbers 1 through 4). Their brighter shading indicates the presence of sp^3 bonding characteristic of crystalline carbon, including NDs. These results, coupled with the previous SAD and FFT analyses, are consistent with NDs and inconsistent graphite, graphene, and copper (see *SI Appendix, EFTEM Analysis*).
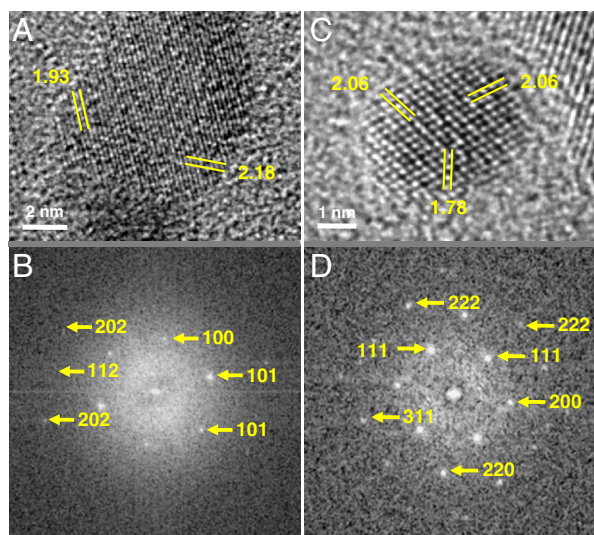
Fig. 8. Crystallographic data for NDs from 2.8 m. (*A*) HRTEM image of monocrystalline nanoparticle identified as lonsdaleite. The (101) and (110) planes are visible with d-spacings of 1.93 and 2.18 Å), respectively. (*B*) FFT of same lonsdaleite crystal above. The values adjacent to each spot indicate the reciprocal lattice vector. Image reveals (101) planes with lattice spacing of 1.93 Å, consistent with lonsdaleite. (*C*) HRTEM image displaying typical lattice spacing of n-diamond. The 1.78 Å measurement represents the (200) planes, consistent with n-diamond. (*D*) FFT of same n-diamond shown above.
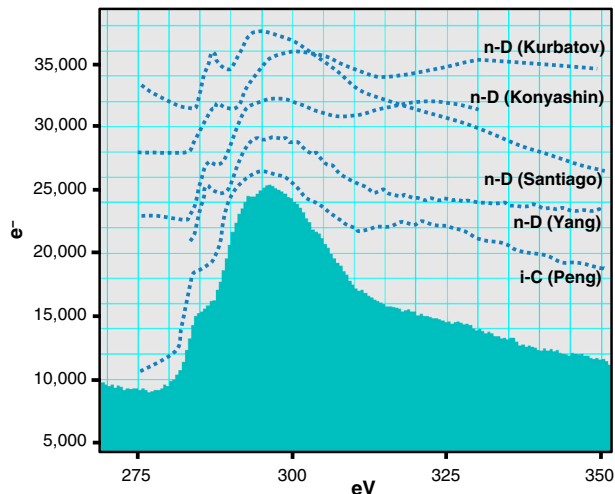
Fig. 9. EELS spectra for NDs from 2.8 m. A typical carbon peak of approximately 295–300 eV shows that the particle is carbon. Published n-diamond and i-carbon spectra (dotted lines) are shown for comparison (4, 32, 36, 37).

Twinned NDs. These NDs are made up of two or more crystals that share a common lattice plane (the twin plane) and grow symmetrically away in different orientations (Fig. 11). Twinning is commonly observed in commercial NDs formed by carbon vapor deposition (CVD), during which NDs crystallize from gaseous carbon, typically at high temperatures in an inert atmosphere. Twinned cubic NDs are common in meteorites (38), having formed in space through a process possibly analogous to CVD (39). They also are found in impact craters (39)[‡‡], where they formed upon impact from terrestrial carbon. Twinned lonsdaleite has been observed in meteorites and associated with impact craters[‡‡]. Twins can form in numerous configurations, including "accordion twins," which exhibit folded, pleat-like lattice planes, and fivefold "star twins" (38), as observed by Tian et al. (14) in the YDB layer from Lommel, Belgium. At Cuitzeo, most NDs were twinned n-diamond and i-carbon and only occasionally were monocrystalline NDs observed. Twinned lonsdaleite with d-spacings of 2.06 Å and 1.93 Å was observed occasionally (Fig. 11*B*).

Cubic NDs. Cubic NDs were previously identified in the YDB (2–4), and subsequently, Tian et al. (14) confirmed cubic NDs in the YDB. In the Cuitzeo section, however, we could not unequivocally identify the cubic allotrope. This may be due to masking by i-carbon and/or n-diamonds, which share some d-spacings with cubic NDs (*SI Appendix,* Table 8). Also, cubic NDs possess so-called "forbidden reflections," such as the 1.78 Å d-spacing, that are typically invisible in cubic SAD patterns but are sometimes apparent in twinned cubic NDs, most likely due to double diffraction (38). Because n-diamonds also display these forbidden reflections, twinned n-diamonds cannot be easily differentiated from twinned cubic NDs. Thus, it is possible that some of the apparent n-diamonds from Cuitzeo are actually twinned cubic NDs.

Carbon Onions and Ribbons. In the YDB at Lommel, Belgium, Tian et al. (14) observed carbon onions, nanonmeter-sized nanoparticles constructed of concentric carbon shells. Carbon onions typically are comprised of three to eight closed shells, ranging from 3 to 100 nm wide (40), and may be either hollow or contain NDs. Broken and whole carbon onions, ranging from ovoid to round and from 2 to 10 nm wide, were observed in the 2.75 m sample using HRTEM imaging (Fig. 12; *SI Appendix,* Fig. 10). These display carbon shells with variable spacings, ranging from

[‡‡]Masaitis VL, Impact diamonds from astroblemes, Mineralogical Society of America 1996 Spring Meeting, May 20—24, 1996, Baltimore, MD, abstract supplement to Eos Transactions, S142–S143.

Fig. 10. EFTEM maps of NDs. (*A*) An inverted "zero-loss" image displaying brighter nanoparticles (numbered). Inset shows 4-nm-wide nanoparticle number 1 that exhibits crystalline lattice spacings of 1.30 and 2.12 Å, consistent with i-carbon. Resolution is low due to surrounding amorphous carbon. (*B*) A map of particles detected with characteristic carbon signature at 299 ± 5 eV. Brighter particles at numbers 1 through 4 correspond to the *Left* panel, indicating sp³ bonding typical of NDs. Darker area near number 3 is due to sp² bonding in the amorphous carbon film.

approximately 3.47 to 4.37 Å with an average of 4.07 Å. Although it is not possible to identify the exact carbon allotrope, these spacings are somewhat consistent with fullerenes (4.09 Å), which were previously detected in the YDB layer in North America (1). About half of the carbon onions enclose apparent polycrystalline i-carbon, as measured by FFT. However, definitive analysis is not possible because the NDs are very small and surrounded by amorphous carbon and carbon onion shells.

Because natural wildfires can produce carbon onions, Tian et al. (14) postulated that YDB NDs may have formed during wildfires by high-pressure compression within carbon onions. However, there is no evidence to support that suggestion because no naturally formed carbon onions have ever been found to contain NDs (*SI Appendix,* Fig. 11 and *Carbon Onions*). On the other hand, diamond-bearing carbon onions are known to form during production of NDs by trinitrotoluene (TNT) detonation (41) under high temperatures and oxygen-deficient conditions that are known to occur during an impact event, as discussed below.

We also observed carbon ribbons, which are multinanometer-long parallel chains of carbon atoms found in interstellar dust particles, or IDPs, and meteorites (42) (*SI Appendix,* Fig. 10). They have also been observed in nanodiamond-rich residues from TNT detonation (41).

Fig. 11. HRTEM images of twinned NDs from the 2.8 m layer. Double yellow lines represent lattice planes and the numbers indicate d-spacings in Å. Arrows are parallel to common twinning plane. (*A*) Star-twin ND with fivefold star-like morphology. (*B*) Accordion twin lonsdaleite with pleated morphology. (*C*) Twin with multiple folds. (*D*) "Scalloped" twin.

Fig. 12. Carbon onions from 2.75 m. (*A*) HRTEM image displays 10 nm carbon onion. Parallel strands nearby appear to be carbon ribbons. (*B*) Drawing illustrates shells of carbon onion and nanoparticle shown in *A*. (*C*) FFT of enclosed crystal with d-spacings generally consistent with i-carbon but with insufficient resolution to be definitive.

Discussion

Multiple hypotheses have been proposed to explain YDB markers. Nearly all can be rejected, as follows:

"Cosmic Rain." Several workers have speculated that YDB MSp and NDs represent the normal "cosmic rain" that falls continuously from space (6, 13, 27). This is a testable hypothesis, but those authors conducted no such tests. For Cuitzeo, we analyzed all available MSp geochemically and compared them to >700 meteorites and cosmic spherules from Greenland, Antarctica, and elsewhere (Fig. 6). The MSp geochemistry indicates that they are noncosmic and, instead, appear to be melted terrestrial material. Furthermore, the high abundance of YDB MSp indicates that cosmic rain is an unlikely cause because cosmic spherules in sediment are very rare. For example, the 1991 EUROMET Antarctic micrometeorite collection from continuously deposited ice contains only 0.015 microspherules (50–100 μm) per kg of ice (1 L) (43). In contrast, Cuitzeo contains >2,000 MSp per kg, totalling 130,000 × more for the same sample weight.

Cosmic NDs occur in meteorites and cosmic dust, but Tian et al. (14) concluded that YDB NDs are not cosmic because they display $\delta^{13}C$ abundances (−28.1 to −26.3‰) that are terrestrial. Their work confirmed the results of Bunch et al.,[§§] who reported isotopic analyses on diamond-rich residue from 12 YDB sites that exhibited terrestrial values for $\delta^{13}C$ (−30 to −22‰) and $\delta^{15}N$ (−17 to 15‰). Furthermore, these values are similar to those for NDs in the Cretaceous–Paleogene boundary layer (KPg, formerly K-T), where Gilmour et al. (44) measured $\delta^{13}C$ (−18‰) and $\delta^{15}N$ (6‰) and concluded that KPg NDs were formed during impact from terrestrial material, most likely from carbon-rich target rocks. Isotopic analyses of the carbon-rich YDB interval at Cuitzeo yielded values ranging from −23 to −19‰ for $\delta^{13}C$ consistent with the formation of Cuitzeo NDs from terrestrial, not cosmic, carbon.

Wildfires. Typical wildfire temperatures range from approximately 900 to 1,200 °C with the highest reported being 1,450 °C (45). These temperatures are too low to melt magnetite into MSp (1,540 °C) and too high for the survival of NDs, which combust between 400 and 600 °C (39). Neither proxy has been reported in normal wildfires. This conclusion is reinforced by our observation that the Cuitzeo 3.1 m peak in charcoal is indicative of a major wildfire episode, and yet, displays low levels of MSp, CSp, or NDs (Fig. 4; *SI Appendix,* Table 5). Another indication that the YDB proxies are not wildfire-related is that marker peaks (2.80 to 2.75 m) were deposited earlier than the wildfire charcoal peak (2.70 to 2.65 m).

[§§]Bunch TE, West A, Wittke J, Kennett JP, New physical evidence for a cosmic impact with the Earth at 129 ka, American Quaternary Association (AMQUA) 5, August 12–15, 2010, Laramie, WY, paper #3.

Volcanism. Low-energy volcanism produces silicate spherules but does not distribute them widely (46). Conversely, high-energy eruptions capable of disseminating ejecta widely do not appear to produce spherules. For example, the Toba eruption at approximately 75 ka, one of the largest of the last 5 million years, ejected debris up to 2,000 km, yet no spherules have been detected (46). Likewise, we analyzed tephra samples from the Laacher See eruption layer in Germany that preceded the YD onset and found no MSp or NDs. On the other hand, the Cuitzeo YDB layer contains almost no volcanic material; the closest volcanic layers are approximately 18 kyr earlier and approximately 8 kyr later (15), indicating that no significant local volcanic eruptions occurred near 12.9 ka.

Anthropogenesis. NDs have never been reported in industrial by-products, and because MSp, CSp, and NDs are deeply buried at approximately 3 m in well-stratified deposits at Cuitzeo, there was no reasonable chance for human contamination.

Potential Misidentification of Markers. Surovell et al. (6) reported finding no YDB MSp peaks, although claiming to follow the protocol of Firestone et al. (1) for quantification of MSp, and concluded that Firestone et al. misidentified and/or miscounted the MSp. Later, Lecompte et al.[¶¶] independently examined two YDB sites common to Firestone et al. and Surovell et al. They reported that "spherule abundances are consistent with those of Firestone et al." and "inconsistent with the results of Surovell et al." They also concluded that Surovell et al. altered the prescribed MSp protocol in fatal ways, particularly by not observing requirements for sample thickness, sample weight, and size sorting. We consider these discrepancies significant enough to negate the conclusions of Surovell et al. (*SI Appendix, Surovell et al.*).

Daulton et al. (8) found no YDB NDs at Arlington Canyon, California, or at Murray Springs, Arizona, as earlier reported in Kennett et al. (2, 3). They searched for NDs in "microcharcoal aggregates" from the Murray Springs YDB site and, finding none, claimed to refute the previous results. However, Kennett et al. never claimed to find NDs in charcoal, and instead, observed NDs at Murray Springs in acid-resistant residues from bulk sediment (2, 3), which Daulton et al. did not investigate.

Daulton et al. (8) further speculated that Kennett et al. (2, 3) misidentified YDB NDs, observing copper instead, which displays d-spacings nearly identical to n-diamond and i-carbon. In addition, Daulton et al. pointed out that graphene and/or graphane have d-spacings similar to lonsdaleite and that the lonsdaleite diffraction pattern reported from Arlington Canyon by the Kennett et al. (2) was missing the lonsdaleite diffraction line at 1.93 Å. However, in YD-aged ice in Greenland, Kurbatov et al. (4) identified lonsdaleite with the 1.93- Å line, which definitively demonstrates that those Greenland nanoparticles cannot be graphene or graphane. At Lake Cuitzeo, numerous NDs have been identified with the 1.93 Å (101) line, as shown in Fig. 8 *A* and *B* and Fig. 11*B*, eliminating the possibility that these crystals are graphene or graphane. SAD and all other analyses conclusively show that the Cuitzeo nanoparticles analyzed have d-spacings consistent with lonsdaleite and other NDs. In independent support of NDs in the YDB, Tian et al. (14) and Van Hoesel[‡] identified cubic NDs in the YDB layer in Europe.

Regarding CSp, Scott et al. (7) speculated that those found at YDB sites (1–3) are simply charred fungal sclerotia, which are ball-like clusters of long, branching filamentous structures, common to some fungi. The CSp from Cuitzeo and other YDB sites are unmistakably different from sclerotia in numerous critical characteristics. In particular, charred and uncharred sclerotia have textured, filamentous, low-reflectivity interiors, whereas at Cuitzeo, SEM imaging demonstrates that CSp have smooth, glassy, highly reflective interiors with no evidence of filamentous structure observed in fungal sclerotia (or cellular structure found in charcoal) (*SI Appendix,* Fig. 5).

Cuitzeo CSp also contain numerous noncarbon particles, including aluminosilicates, indicating that these cannot be primary biological entities, such as sclerotia. In support of this, several lines of evidence support the formation of CSp during biomass burning. For example, Firestone et al. (1) reported the production of CSp in modern wildfires, and laboratory experiments have demonstrated the production of CSp from charred tree resin at approximately 500 °C[***]. These CSp are morphologically identical to those found in the YDB but contain no NDs. Also, CSp similar to those found in the YDB have been reported by Harvey et al. (47), who observed vesicular CSp in the impact layer at the KPg, and suggested that CSp, along with aciniform soot, formed during impact into carbon-rich target rocks.

Cosmic Impact as Only Viable Hypothesis

Impact-related CVD. Tian et al. (14) speculated that YDB NDs formed by CVD, although they offered no details. In the laboratory, formation of NDs by CVD requires intense heating of carbon vapor within an inert atmosphere, conditions not known to exist naturally at Earth's surface [*SI Appendix, CVD (Carbon Vapor Deposition)*]. ET impacts are the only known natural events capable of generating CVD-like conditions under a reduced-oxygen atmosphere (39). This CVD mechanism has been proposed for the KPg, where $\delta^{13}C$ and $\delta^{15}N$ values for cubic NDs suggest they formed from carbon that is terrestrial and not cosmic (44).

Comets. Based upon astrophysical observations and modeling, Napier (48) proposed that YDB impact markers were produced when Earth encountered a dense trail of material from a large already fragmented comet. His model predicts cluster airbursts and/or small cratering impacts that could account for the wide distribution of YD impact debris across more than 10% of the planet, including Cuitzeo. Most comets eventually break up as they transit the inner solar system, and previously unknown fragmented comets are discovered by space-borne telescopes, such as the Solar and Heliospheric Observatory, on average every 4 y. As evidence, Earth is bombarded at an average rate of once every 5 d by one of 72 meteor streams or "showers," massive clouds of debris from fragmented comets. These well-known meteor showers, e.g., Perseids, Geminids, Taurids, etc., are highly dispersed, but in the recent geologic past, each stream was far more condensed, containing many large, potentially destructive fragments. Currently, the Taurid Complex contains 19 large near-earth Apollo asteroids, with diameters ranging from approximately 1.5 km (6063 Jason) to approximately 5 km (4184 Cuno) (48). None of these currently threatens Earth but may do so in the future.

Impact Dynamics. Earth has been subjected to a continuous, although intermittent bombardment by impactors with diameters ranging from microns to tens of kilometers; velocities range from approximately 11 km/s to 73 km/s with typical values of 17 km/s for asteroids and 51 km/s for comets. The term "cosmic impact" evokes images of craters ranging from the 50-kyr-old, 1-km-diameter Meteor Crater to the 2-billion-year-old, 200-km-diameter Vredefort crater (49, 50). For these crater-forming events that have peak impact pressures in the range of hundreds of GPa, impact dynamics and shock wave metamorphic effects are well understood (49, 50). An ET impact is the only natural mechanism known to produce major coeval abundances in cubic NDs, lons-

¶¶LeCompte MA, et al., Summary of unusual material in early Younger Dryas age sediments and their potential relevance to the YD Impact Hypothesis, INQUA XVIII, July 21–27, 2011, Bern Switzerland, (abstr.) 1813.

***Kimbel D, West A, Kennett JP, A new method for producing nanodiamonds based on research into the Younger Dryas extraterrestrial impact, AGU Fall Meeting, December 15–19, 2008, Eos Trans. AGU, 90(52), Fall Meet. Suppl., #PP13C-1470.

daleite, and quench-melted MSp, both of which co-occur in impact events, including Ries crater and the KPg (39).

Based on hundreds of shock-recovery experiments by one of the authors of this article (DeCarli), the formation of lonsdaleite in graphite-bearing gneisses in the Ries, Popigai, and other impact craters is in complete accord with static high-pressure data on solid–solid transformation of graphite to lonsdaleite and cubic NDs (29–31). However, this transformation does not readily explain the NDs found at the KPg boundary or in the YDB. Based on available evidence, it seems unlikely that the YDB NDs formed by shock compression of terrestrial graphite, and instead, our preferred mechanism invokes the interaction of an ET object with Earth's atmosphere (49). If incoming objects are relatively small, virtually all kinetic energy is transferred to the atmosphere at high altitudes, creating an air shock with temperatures up to tens of thousands degrees Kelvin. These are the familiar shooting stars, the remains of which may be collected as cosmic dust. Although shock pressures due to solid–air interaction are modest at high altitudes, larger objects may be disrupted and fragmented as pressure builds due to increasing atmospheric density at lower altitudes. This breakup is especially likely if the object was loosely consolidated or low density like a comet. When an incoming ET object encounters the atmosphere and breaks apart, individual pieces rapidly decelerate due to the marked increase in the ratio of cross-sectional area to mass. Area of the luminous air shock is correspondingly increased, with the result that the object appears to "explode" in a fireball. For an object traveling at 30 km/s, air shock pressure would be approximately 20 MPa at 20 km altitude, approximately 170 MPa at 10 km, and approximately 900 MPa at sea level. For an air shock of 170 MPa, the pressure exceeds unconfined compressive strengths of many rocks.

These energetic events are often termed "atmospheric impacts" to distinguish them from more familiar crater-forming events. For example, the craterless Tunguska event in Siberia in 1908 appears to be such an atmospheric impact. Estimates of energy associated with this event range from 3 to 24 megatons of TNT (51, 52), powerful enough to produce an air shock that leveled approximately 80 million trees across 2,000 km^2 of forest. At a distance of 60 km, the air shock was still able to knock down a Siberian trader (53), and thermal radiation was intense enough to char his clothing (49). Even though the Tunguska atmospheric impact formed no known crater, it produced MSp (54) and lonsdaleite (55). Studies of such atmospheric impacts indicate that Tunguska-sized events up to 24 megatons occur about once every 220 y (52). Similar but smaller effects occurred during the Trinity atomic bomb test in 1945, an aerial burst that also left no crater yet produced glassy surficial sheet melt, along with rounded and teardrop-like glassy spherules (56). Such an atmospheric impact scenario is also the best explanation for other well-known events with no known craters, including the Libyan Desert glass field and Dakhleh Oasis glass in Egypt. In the Australasian tektite field (780 ka), microspherules and tektites are strewn across 10–30% of Earth's surface, producing the world's largest ejecta field and yet, there is no known crater. Wasson (57) proposed that the Australasian field resulted from an atmospheric impact by a comet approximately 1 km in diameter, striking Earth's atmosphere at an oblique angle.

The amount of kinetic energy transferred during an atmospheric impact via air shock depends upon the cross-sectional area of the object, its velocity, and its mass. Air shock pressure depends upon the velocity of the object and the density of air at altitude. Shock front temperature is limited to approximately 20,000 K by dissociation of air molecules ahead of front (58), and effective duration of the intense thermal pulse can be of the order of seconds. Whether an object disintegrates in flight depends upon its strength, size, shape, velocity, and angle of entry. In the case of a comet that is a dusty porous snowball having little strength, a 20-km-diameter comet traveling at 40 km/s

would not disintegrate in the Earth's atmosphere; the front of the comet would impact Earth before the shock from atmospheric impact reached the rear of the comet. However, comets with dimensions of tens of meters will disintegrate at high altitude. Weissman (59) estimated that a comet would have to be >350 m in diameter to penetrate Earth's atmosphere and form a crater, depending upon angle, velocity, etc. Such an event would be at least 500 × more energetic than the Tunguska event.

YD Impact Model. Based on current data, we propose the following preliminary model for formation of the YDB NDs and MSp. A comet or asteroid, possibly a previously fragmented object that was once greater than several hundred meters in diameter, entered the atmosphere at a relatively shallow angle (>5° and <30°). Thermal radiation from the air shock reaching Earth's surface was intense enough to pyrolyze biomass and melt silicate minerals below the flight path of the impactor (60). Pyrolytic products were oxidized, locally depleting the atmosphere of oxygen, and within microseconds, residual free carbon condensed into diamond-like crystal structures, CSp, carbon onions, and aciniform soot. This involved a CVD-like process similar to diamond-formation during TNT detonation. In some cases, carbon onions grew around the NDs and other nanomaterials. At the same time, iron-rich and silicate materials may have melted to form MSp.

Several seconds later, depending on the height of the thermal radiation source, the air shock arrived. NDs, MSp, CSp, and other markers were lofted by the shock-heated air into the upper atmosphere, where prevailing winds distributed them across the Northern and Southern Hemispheres. We suggest that the above model can account for the observed YDB markers.

Methods

Core samples were divided into multiple aliquots for a wide range of analyses. Details on methodology followed the protocol published in Firestone et al. (2007), along with improvements as discussed in detail in the manuscript and in *SI Appendix, Methods*. These include MSp, magnetic grains, framboidal spherules, magnetic glass, aciniform soot, pollen, diatoms, charcoal, and CSps. NDs were extracted using the procedure published in Kennett et al. (2), as further discussed in the manuscript and in *SI Appendix, Methods*. Standard procedures were followed for analyses of all proxies.

Summary

Synchronous peaks in multiple YDB markers dating to 12.9 ka were previously found at numerous sites across North and South America and in Western Europe. At Lake Cuitzeo, magnetic impact spherules, CSps, and NDs form abundance peaks within a 10 cm layer of sediment that dates to the early part of the YD, beginning at 12.9 ka. These peaks coincide with anomalous environmental, geochemical, and biotic changes evident at Lake Cuitzeo and in other regional records, consistent with the occurrence of an unusual event. Analyses of YDB acid-resistant extracts using STEM, EDS, HRTEM, SAD, FFT, EELS, and EFTEM indicate that Lake Cuitzeo nanoparticles are dominantly crystalline carbon and display d-spacings that match various ND allotropes, including lonsdaleite. These results are consistent with reports of abundant NDs in the YDB in North America and Western Europe.

Although the origin of these YDB markers remains speculative, any viable hypothesis must account for coeval abundance peaks in NDs, magnetic impact spherules, CSps, and charcoal in Lake Cuitzeo, along with apparently synchronous peaks at other sites, spanning a wide area of Earth's surface. Multiple hypotheses have been proposed to explain these YDB peaks in markers, and all but one can be rejected. For example, the magnetic impact spherules and NDs cannot result from the influx of cosmic material or from any known regular terrestrial mechanism, including wildfires, volcanism, anthropogenesis, or alternatively, misidentification of proxies. Currently, only one known event, a cosmic impact, can explain the diverse, widely distributed assemblage of proxies. In the entire geologic record, there are

only two known continent-wide layers with abundance peaks in NDs, impact spherules, CSps, and aciniform soot, and those are the KPg impact boundary at 65 Ma and the YDB boundary at 12.9 ka.

1. Firestone RB, et al. (2007) Evidence for an extraterrestrial impact 12,900 years ago that contributed to the megafaunal extinctions and the Younger Dryas cooling. *Proc Natl Acad Sci USA* 104:16016–16021.
2. Kennett DJ, et al. (2009) Shock-synthesized hexagonal diamonds in Younger Dryas boundary sediments. *Proc Natl Acad Sci USA* 106:12623–12628.
3. Kennett DJ, et al. (2009) Nanodiamonds in the Younger Dryas boundary sediment layer. *Science* 323:94.
4. Kurbatov AV, et al. (2010) Discovery of nanodiamond-rich layer in the Greenland ice sheet. *J Glaciol* 56:749–759.
5. Anderson DG, Goodyear AC, Kennett JB, West A (2011) Multiple lines of evidence for possible human population decline/settlement reorganization during the early Younger Dryas. *Quatern Int* 242:570–583.
6. Surovell TA, et al. (2009) An independent evaluation of the Younger Dryas extraterrestrial impact hypothesis. *Proc Natl Acad Sci USA* 106:18155–18158.
7. Scott AC, et al. (2010) Fungus, not comet or catastrophe, accounts for carbonaceous spherules in the Younger Dryas "impact layer". *Geophys Res Lett* 37:L14302.
8. Daulton T, Pinter N, Scott A (2010) No evidence of nanodiamonds in Younger-Dryas sediments to support an impact event. *Proc Natl Acad Sci USA* 107:16043–16047.
9. Kerr RA (2010) Mammoth-killer impact flunks out. *Science* 329:1140–1141.
10. Mahaney WC, Krinsley D, Kalm V (2010) Evidence for a cosmogenic origin of fired glaciofluvial beds in the northwestern Andes: Correlation with experimentally heated quartz and feldspar. *Sediment Geol* 231:31–40.
11. Mahaney WC, et al. (2010) Evidence from the northwestern Venezuelan Andes for extraterrestrial impact: The black mat enigma. *Geomorphology* 116:48–57.
12. Mahaney WC, et al. (2011) Fired glaciofluvial sediment in the northwestern Andes: Biotic aspects of the Black Mat. *Sediment Geol* 237:73–83.
13. Haynes CV, Jr, Lauretta DS, Ballenger JAM (2010) Reply to Firestone et al: No confirmation of impact at the lower Younger Dryas boundary at Murray Springs AZ. *Proc Natl Acad Sci USA* 107:E106–E106.
14. Tian H, Schryvers D, Claeys P (2010) Nanodiamonds do not provide unique evidence for a Younger Dryas impact. *Proc Natl Acad Sci USA* 108:40–44.
15. Israde-Alcántara I, et al. (2010) Evolución paleolimnologica del Lago Cuitzeo, Michoacán, durante el Pleistoceno–Holoceno (Paleolimnologic evolution of Lake Cuitzeo, Michoacán, during the Pleistocene–Holocene). *B Soc Geol Mex* 62:345–357.
16. Pradal E, Robin C (1994) Long-lived magmatic phases at Los Azufres volcanic center. *Mexico J Volcan and Geotherm Res* 63:201–215.
17. Islebe GA, Hooghiemstra H (2006) Effects of the Younger Dryas cooling event on late Quaternary montane oak forest in Costa Rica. *Ecology and Conservation of Neotropical Montane Oak Forests*, ed M Kappelle (Springer, Berlin, Heidelberg), pp 29–37.
18. Hodell DA, et al. (2008) An 85-ka record of climate change in lowland Central America. *Quat Sci Rev* 27:1152–1165.
19. Correa-Metrio A (2010) Cimate and vegetation of the Yucatan Peninsula during the Late Pleistocene. PhD dissertation (Florida Institute of Technology, Melbourne FL), p 194.
20. Hooghiemstra H, Cleef AM, Noldus CW, Kappelle M (1992) Upper Quaternary vegetation dynamics and palaeoclimatology of the La Chonta bog area (Cordillera de Talamanca, Costa Rica). *J Quaternary Sci* 7:205–225.
21. Bush MB, et al. (1992) A 14,300-yr paleoecological profile of a lowland tropical lake in Panama. *Ecol Monogr* 62:251–275.
22. Alley RB (2000) The Younger Dryas cold interval as viewed from central Greenland. *Quat Sci Rev* 19:213–226.
23. Haug GH, Hughen KA, Peterson LC, Sigman DM, Röhl U (2001) *Cariaco Basin Trace Metal Data* (NOAA/NGDC), IGBP PAGES/World Data Center A for Paleoclimatology Data Contribution Series #2001 12628.
24. Piper DZ, Dean WE (2002) *Trace-Element Deposition in the Cariaco Basin, Venezuela Shelf, under Sulfate-Reducing Conditions: A History of the Local Hydrography and Global Climate, 20 ka to the Present* (USGS, Washington, DC), Prof. paper 1670.
25. Haynes CV, Jr (2008) Younger Dryas "black mats" and the Rancholabrean termination in North America. *Proc Natl Acad Sci USA* 105:6520–6525.
26. Zarate-del-Valle PF, Rushdi AI, Simoneit BRT (2006) Hydrothermal petroleum of Lake Chapala, Citala Rift, western Mexico: Bitumen compositions from source sediments and application of hydrous pyrolysis. *Appl Geochem* 21:701–712.
27. Pinter N, et al. (2011) The Younger Dryas impact hypothesis: A requiem. *Earth Science Reviews* 106:247–264.
28. Wilkin RT, Barnes HL (1997) Formation processes of framboidal pyrite. *Geochim Cosmochim Acta* 61:323–339.
29. DeCarli PS, Jamieson JC (1961) Formation of diamond by explosive shock. *Science* 133:1821–1822.
30. DeCarli PS (1966) *US Patent* 3,238,019.
31. DeCarli PS, Bowden E, Jones AP, Price GD (2002) Laboratory impact experiments versus natural impact events. *Geo S Am S* 356:595–605.
32. Peng JL, Orwa JO, Jiang B, Prawer S, Bursill LA (2001) Nano-crystals of c-diamond, n-diamond and i-carbon grown in carbon-ion implanted fused quartz. *Int J Mod Phys B* 15:3107–3123.
33. Wen B, Zhao J, Li T, Dong C, Jin J (2006) Time-evolutional X-ray diffraction of n-diamond: An intermediate state between fcc and diamond structure. *Diam Relat Mater* 15:1323–1328.
34. Konyashin I, et al. (2006) A new hard allotropic form of carbon: Dream or reality? *Int J Refract Metals Hard Mater* 24:17–23.
35. Hirai H, Kondo K-I (1991) Modified phases of diamond formed under shock compression and rapid quenching. *Science* 253:772–774.
36. Santiago P, Camacho-Bragado GA, Martin-Almazo M, Murgich M, José-Yacaman J (2004) Diamond polytypes in Mexican crude oil. *Energy Fuels* 18:390–5.
37. Yang ZQ, et al. (2008) TEM and Raman characterization of diamond micro- and nanostructures in carbon spherules from upper soils. *Diam Relat Mater* 17:937–943.
38. Daulton TL, Eisenhour DD, Bernatowicz TJ, Lewis RS, Buseck PR (1996) Genesis of presolar diamonds: Comparative high-resolution transmission electron microscopy study of meteoritic and terrestrial nano-diamonds. *Geochim Cosmochim Acta* 60:4853–4872.
39. Hough RM, Gilmour IC, Pillinger T (1998) Impact nanodiamonds in Cretaceous-Tertiary boundary fireball and ejecta layers: Comparison with shock-produced diamond and a search for lonsdaleite. *Meteoritics and Planetary Science* 33:A70.
40. Mostofizadeh A, Li Y, Song B, Huang Y (2011) Synthesis, properties, and applications of low-dimensional carbon-related nanomaterials. *J Nanomater* 2011:1–21.
41. Kuznetsov VL, et al. (1994) Effect of explosion conditions on the structure of detonation soots, ultradisperse diamond, and onion carbon. *Carbon* 32:873–882.
42. Welz S, McNallan MJ, Gogotsi Y (2006) Carbon structures in silicon carbide derived carbon. *J Mater Process Tech* 179:11–22.
43. Maurette M, Pourchete M, Perreau M (1992) The 1991 EUROMET Micrometeorite collection at Cap-Prudhomme, Antarctica. *Meteoritics* 27:473–475.
44. Gilmour I, et al. (1992) Terrestrial carbon and nitrogen isotopic ratios from Cretaceous-Tertiary boundary nanodiamonds. *Science* 258:1624–6.
45. Philpot CW (1965) *Temperatures in a Large Natural-Fuel Fire* (US. Forestry Service), Research Note PSW-90.
46. Smit J (1990) Meteorite impact, extinctions and the Cretaceous-Tertiary boundary. *Geologie en Mijnbouw* 69:187–204.
47. Harvey MC, Brassell SC, Belcher CM, Montanari A (2008) Combustion of fossil organic matter at the Cretaceous-Paleogene (K-P) boundary. *Geology* 36:355–358.
48. Napier WM (2010) Palaeolithic extinctions and the Taurid Complex. *Mon Not R Astron Soc* 405:1901–1906.
49. Melosh HJ (1989) *Impact Cratering A Geologic Process* (Oxford Univ Press, New York).
50. French BM, Koeberl C (2010) The convincing identification of terrestrial meteorite impact structures. *Earth Science Reviews* 98:123–170.
51. Chyba CF, Thomas PJ, Zahnle KJ (1993) The 1908 Tunguska explosion: Atmospheric disruption of a stony asteroid. *Nature* 361:40–44.
52. Revelle DO (1997) Historical detection of atmospheric impacts by large bolides using acoustic-gravity waves in near Earth objects. *Annals of the NY Acad Sci*, ed JL Remo 822:284–302.
53. Krinov EL (1960) *Principles of Meteoritics* (Pergamon Press, New York).
54. Florenskiy KP (1963) Preliminary results from the 1961 combined Tunguska meteorite expedition. *Meteoritica* 23:3–29.
55. Kvasnitsa VN, et al. (1979) High-pressure carbon polymorphs in mosses from the Tunguska impact site. *Doklady Ukrainskoi Akademii Nauk, B* 12:1000–1004.
56. Eby N, Hermes R, Charnley N, Smoliga JA (2010) Trinitite—the atomic rock. *Geology Today* 26:180–186.
57. Wasson J (2003) Large aerial bursts; an important class of terrestrial accretionary events. *Astrobiology* 3:163–179.
58. Zel'dovich YB, Raiser YP (1966) *Physics of Shock Waves and High-Temperature Hydrodynamic Phenomena* (Academic, New York).
59. Weissman PR (1997) Long-period comets and the Oort cloud, 67–95 in near Earth objects. *Annals of the NY Acad, Sci*, ed JL Remo 822:67–95.
60. Boslough MBE, Crawford DA (2008) Low-altitude airbursts and the impact threat. *Int J Impact Eng* 35:1441–1448.

New Evidence from Central Mexico supporting the Younger Dryas Extraterrestrial Impact Hypothesis

SUPPORTING INFORMATION (click links)

SI FIGURES.

**SI Fig. 1. MAP OF LAKE CUITZEO.** Upper image is a digital elevation model of Lake Cuitzeo in the Mexican State of Michoacán. The lower map shows the lake's location within Mexico with the drainage basin in white area and the coring site in yellow.


SI Fig. 2. SITES OF THIS STUDY: Lake Cuitzeo, Mexico; Lake Petén Itzá, Guatemala; La Chonta Bog, Costa Rica; Lake La Yeguada, Panama; and Cariaco Basin. These sequences display evidence for the YD climate episode although not all regional lakes provide such evidence.
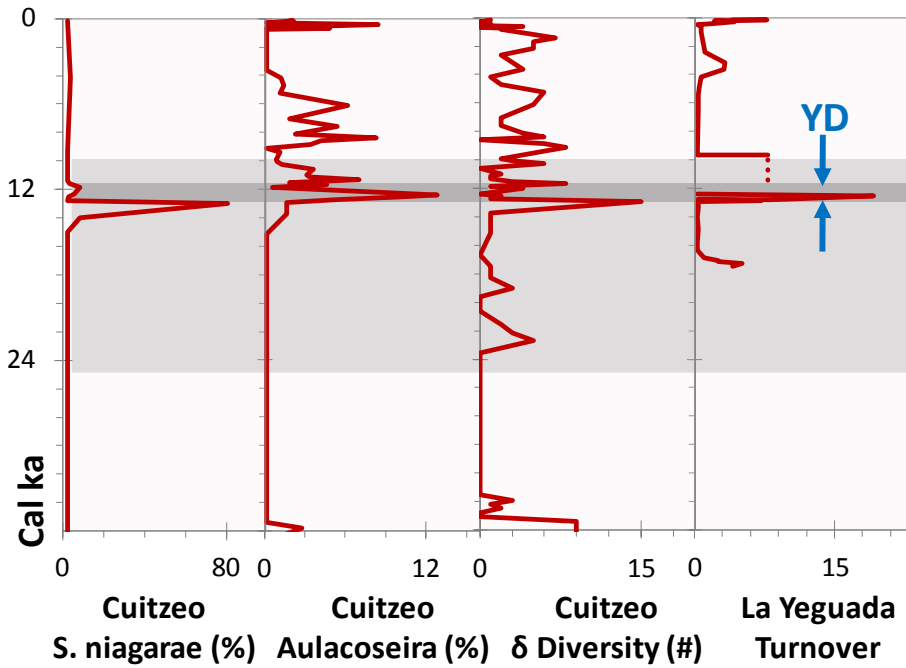
SI Fig. 3. DIATOM RECORDS IN LAKE SEQUENCES. Major diatom peaks in *Stephanodiscus niagarae* and *Aulacoseira* are among the largest and most abrupt in the 27-m Lake Cuitzeo core, and both occur at or near the YD onset. The plot of "δ Diversity" for Lake Cuitzeo represents the differences between total diatom species observed across two consecutive samples; the greatest change occurred at the YD onset at 2.8 m. This closely correlates with the Lake La Yeguada record of species turnover, or rate of change, where the largest ecological change in the 17-kyr record of diatom species occurred at ~12.8 ka (10.8 ^{14}C ka) (Bush *et al.,* 1992). Note: dotted line represents a gap in the record. Light gray band indicates the interval from 4.0 to 2.0 m. Dark gray band between blue arrows indicates the YD episode.
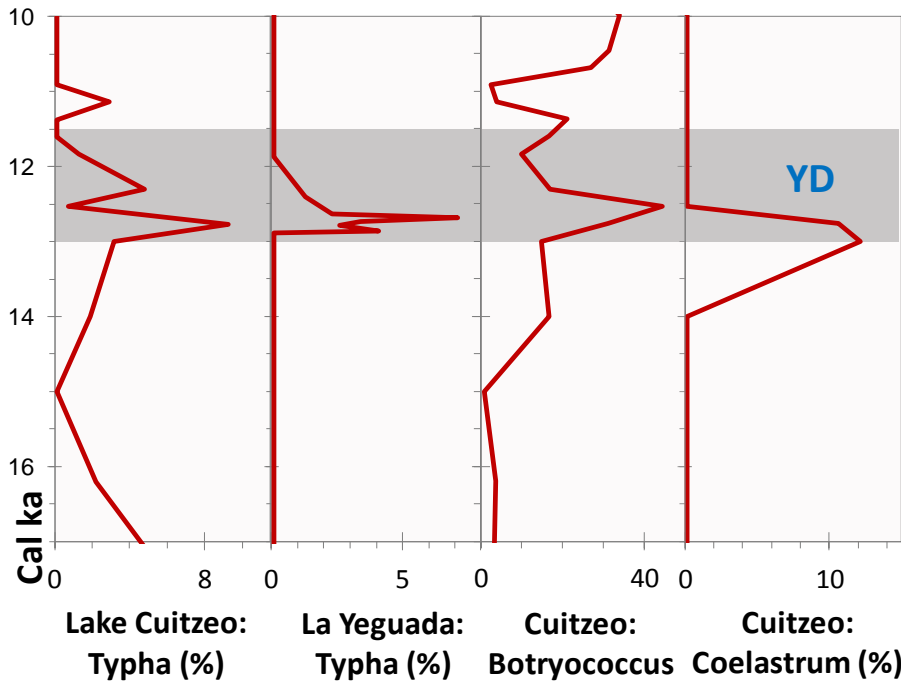
SI Fig. 4. TYPHA and ALGAL RECORDS in LAKE SEQUENCES. The two left-hand graphs display percentages of *Typha* (cattails) pollen for Lakes Cuitzeo and La Yeguada, reaching the highest relative abundances within the 7-kyr record in the early YD. Both were low during the BA and Holocene. The two right-hand graphs display Cuitzeo percentages for two algal taxa. *Coelastrum* reached the largest peak in the 50-kyr record, and *Botryococcus* also increased sharply, indicating major ecological change near the onset of the YD at 12.9 ka.

3
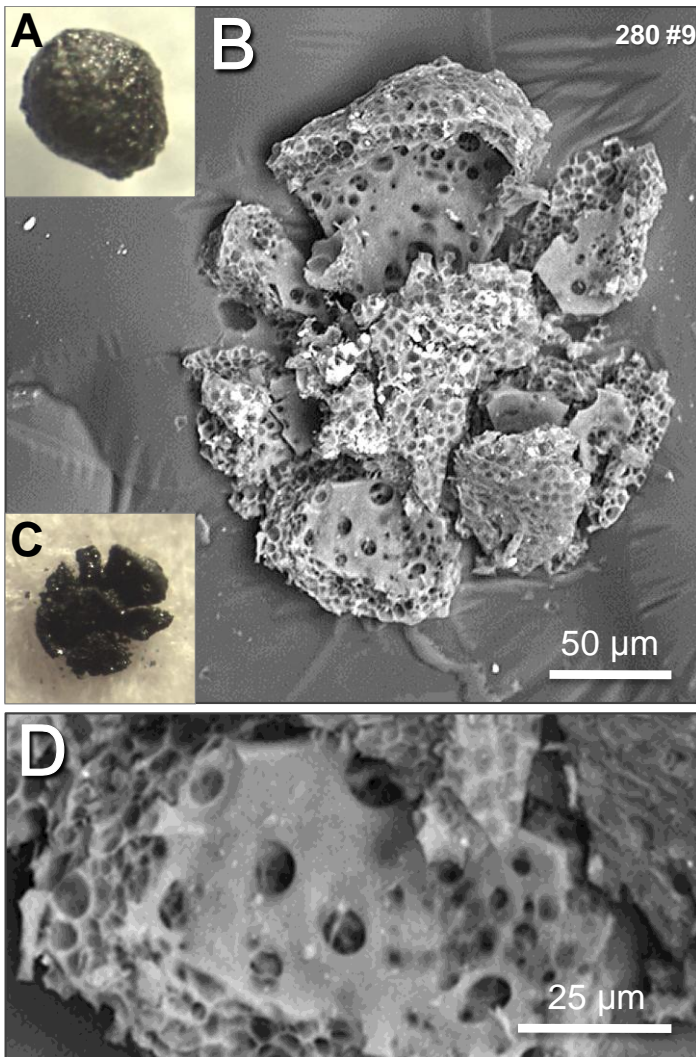
SI Fig. 5. CARBON SPHERULES from the 2.8-m layer. **A)** The upper inset show a whole CSp in reflected light. **B)** SEM image of a crushed CSp; **C)** Photomicrograph of the same crushed CSp. **D)** Closeup of bottom of crushed CSp, illustrating the lack of filamentous texture, as typical of fungal sclerotia, and indicating that these objects are not sclerotia, as speculated by Scott *et al.* (2010).
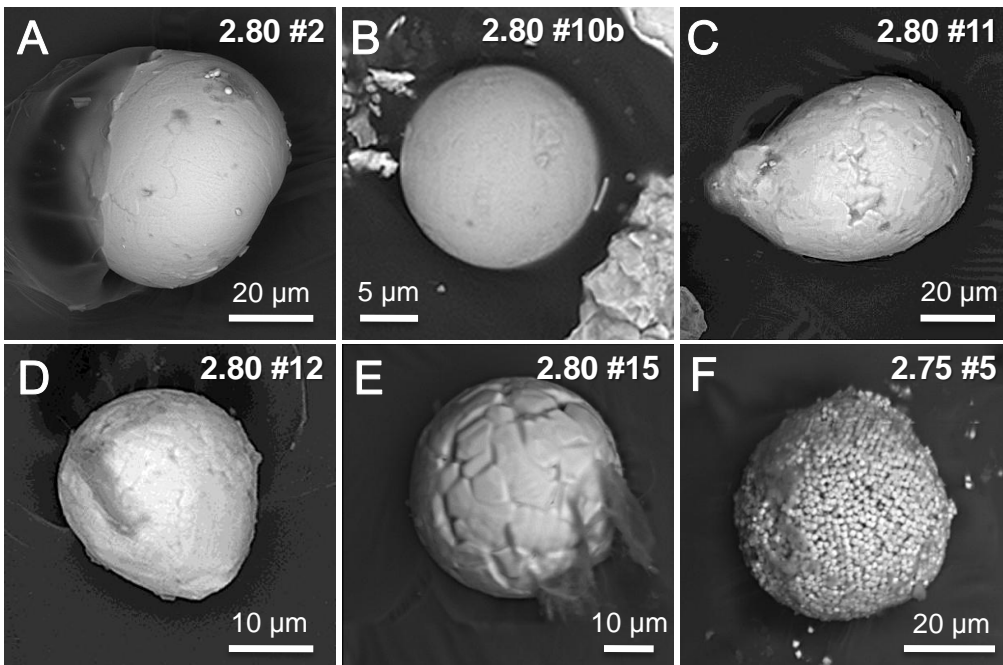
SI Fig. 6. SEM IMAGES OF MAGNETIC PARTICLES.
A) through E) are MSp with quench-melt textures. **B)** & **E)** are spherulitic, but **A), C)** & **D)** are ovoid to elongated, and thus, may not have been tabulated by Surovell *et al.* (2009) (see SI Text-Surovell). **F)** Framboidal spherule. For labels such as "2.80 #2," the "2.80" indicates depth of sample in meters and "#2" is the spherule number listed in SI Table 4.

4
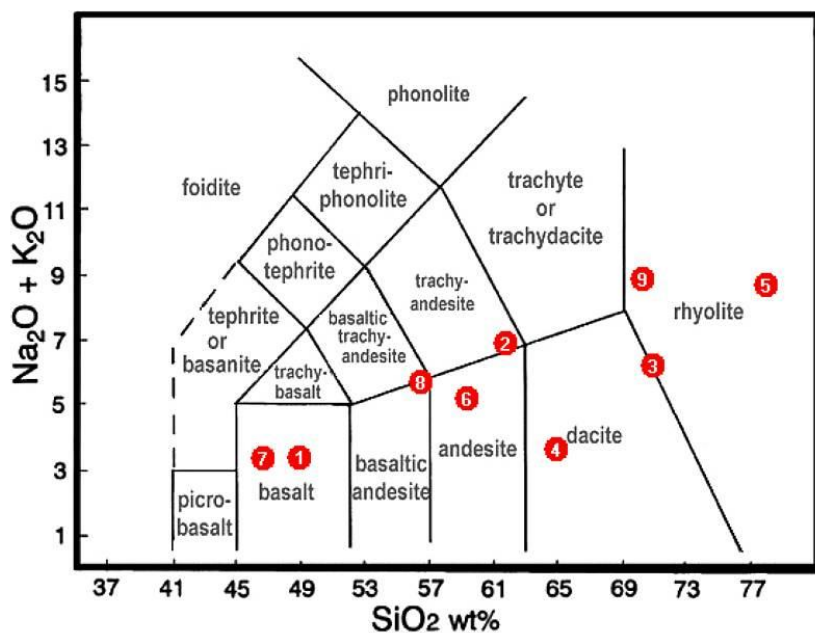
SI Fig. 7. GRAPH comparing total alkali to silica, indicating that the glassy grains are volcanic in origin. Numbers correspond to glassy grains listed in SI Table 4. The quenched MSp do not plot within the limits of this diagram, indicating that none were formed by volcanic processes.
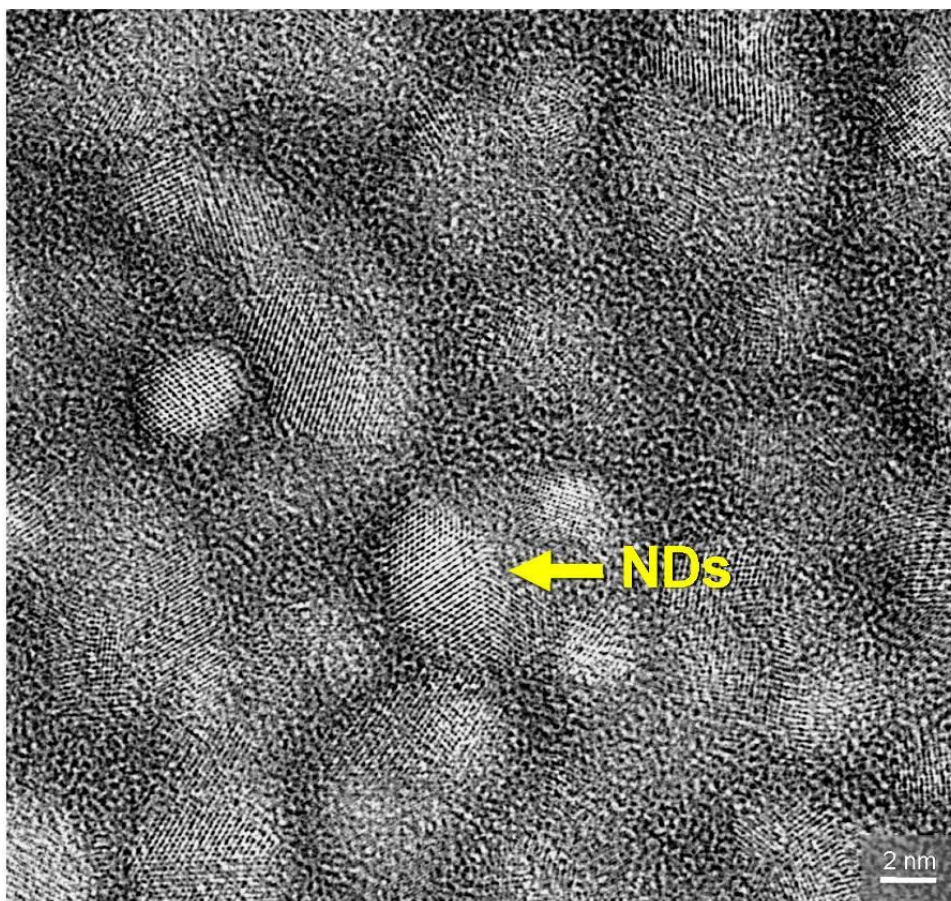
SI Fig. 8. NANODIAMONDS (NDs). Inverted HRTEM image of field of NDs from 2.8 m. NDs are mixed with non-diamond carbon crystals, including carbynes.
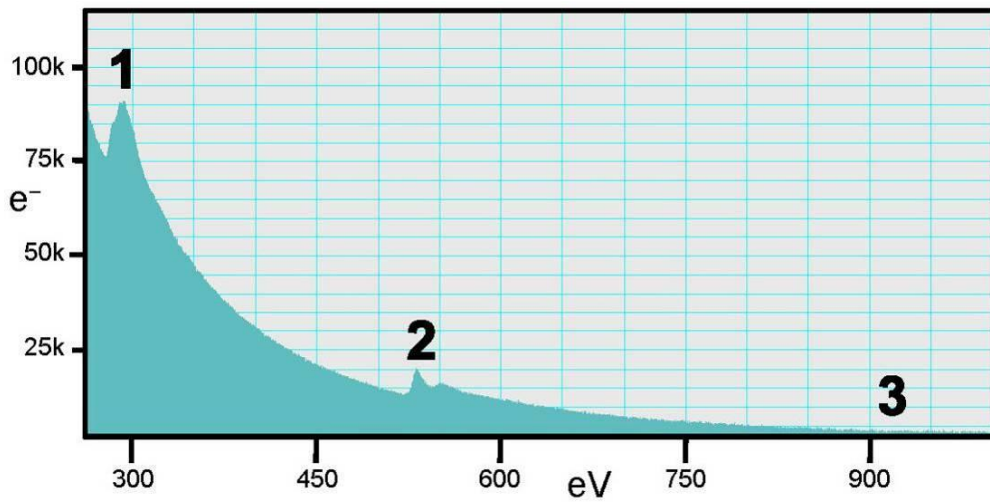
SI Fig. 9. EELS SPECTRUM of a group of nanodiamonds and amorphous carbon from 2.75 m. This confirms the presence of carbon at **#1)** and oxygen at **#2).** No copper was detected near 930 eV at **#3)**, refuting the speculation of Daulton *et al.* (2011) that these particles are copper.
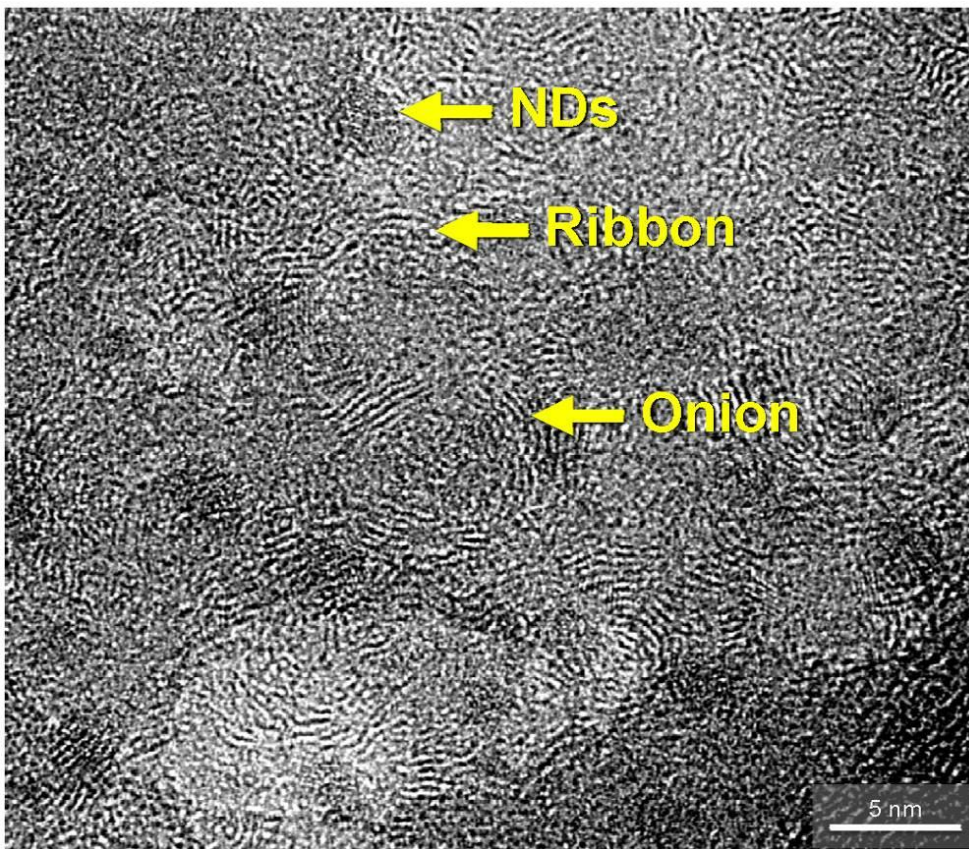
SI Fig. 10. CARBON ONIONS, CARBON RIBBONS and NDs. HRTEM image of a field of onions and ribbons. Darker regions are NDs either within carbon onions or as separate crystals. Material was extracted from the sample at 2.75 m.
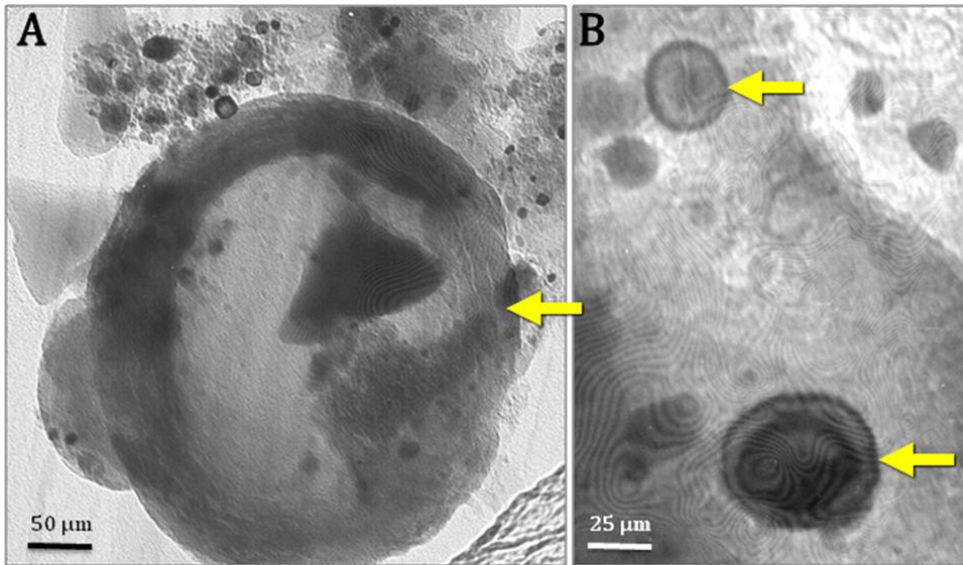
SI Fig. 11. TEM IMAGES OF CARBON ONIONS.

(A) Carbon onion formed from burning wood at ~700°C under wildfire-like conditions in a laboratory experiment (Kimbel, 2008). **(B)** Two carbon onions in charcoal from a modern natural crown-fire near Prescott, AZ. No NDs were found in these onions, which are up to 40,000× larger than the nm-sized carbon onions in Fig. 12 in the main manuscript.

SI TABLES

SI Table 1. AMS ^{14}C DATES on bulk samples from the Lake Cuitzeo core. Samples with "A" and "T" lab numbers were analyzed at the University of Arizona AMS facility. Sample OS 71330 was analyzed at Woods Hole Oceanographic Institute (NOSAMS). WW samples were processed and targets prepared at USGS laboratory in Reston, Virginia and analyzed at Lawrence Livermore National Laboratory AMS facility. Accepted dates are in red, tephra date in black, anomalous dates in blue. Right two columns are the age-depth model in calibrated years from CalPal07 Hulu (Weninger, 2007). The 5th-order polynomial regression formula is y = -5E-$07x^5$ + 6E-$05x^4$ - $0.0025x^3$ + $0.0366x^2$ - 0.0108x + 0.512. R² = 0.946; the r-squared value approaches 1, indicating that the age-depth curve exhibits a strong statistical fit to the data.

Lab number	Depth, (m)	Date, 14C yrs	+/-	Cal BP (CalPal)	+/-	MODEL: Depth, (m)	MODEL: Cal BP (CalPal)
A 9351	0.70	930	55	860	60	0.50	0
A 9352	0.85	1755	115	1690	130	1.00	4500
A9353	1.35	6165	70	7070	90	1.50	7000
A9354	1.95	8830	215	9910	260	2.00	9300
WW 3361	2.05	14720	50	17840	150	2.50	11600
T7-M31	2.25	17605	215	20820	290	2.80	13000
WW 3362	2.45	21730	70	26300	80	3.00	15000
OS 7133C	2.55	21600	100	26180	130	3.50	21000
WW 3363	2.75	27360	130	31970	130	4.00	27500
WW 3375	3.10	32940	190	37240	730	4.50	31000
T11-M47	3.35	15500	130	18810	80	5.00	33500
WW 6422	3.65	23870	100	27850	300	5.50	35500
WW 3576	3.75	28289	120	32710	240	6.00	37000
WW 6423	3.80	29490	190	33880	260	6.50	38500
WW8454	4.00	22780	120	27490	340	7.00	40000
WW8455	4.40	21450	100	25460	220	7.50	41500
AZ 120*	4.70	26800	900	31450	800	8.00	43000
WW8456	5.35	29890	280	34170	240	8.50	44300
A9359	6.10	32565	2885	37350	2950	9.00	46000
WW 3364	6.65	28600	140	33050	260		
A9770	9.10	42400	1000	45540	1100		

SI Table 2. POLLEN DATA for main taxa in Cuitzeo interval from 4.0 to 2.0 m. The YD onset at ~2.8 m. Taxa shown in percent relative abundances. Total pollen shown in grains per gram.

SAMPLE	DEPTH	CAL KA	ALNUS	PINUS	QUERCUS	ABIES	COMPOSITAE	GRAMINEAE	TYPHA	CHENO-AM	CYPERACEAE	TOTAL POLLEN
28	2.00	9.30	12.44	51.67	0.48	15.79	0.00	11.00	0.00	6.22	2.39	26887
29	2.05	9.53	16.57	40.24	1.78	5.92	0.00	23.67	0.00	5.92	5.92	32612
30	2.15	9.99	9.43	54.09	0.63	10.69	0.00	15.09	0.00	6.29	3.77	31909
31	2.25	10.45	7.81	62.50	4.17	3.65	0.00	15.10	0.00	4.17	2.60	33217
32	2.30	10.68	1.44	61.24	2.39	6.70	3.83	19.14	0.00	2.87	2.39	47663
33	2.35	10.91	9.15	47.89	2.11	4.93	5.63	10.56	0.00	10.56	9.15	101777
34	2.40	11.14	3.55	44.68	2.84	3.55	14.89	10.64	2.84	13.48	3.55	707425
35	2.45	11.37	7.57	44.86	9.73	0.00	9.19	19.46	0.00	1.62	7.57	928182
36	2.50	11.60	7.10	59.02	4.92	0.00	0.00	16.39	0.00	3.28	9.29	76512
37	2.55	11.83	4.82	60.24	4.82	0.00	0.00	16.87	1.20	1.20	10.84	138809
38	2.65	12.30	9.02	65.49	3.14	3.53	0.00	6.67	4.71	2.35	5.10	127939
39	2.70	12.53	6.10	78.66	1.83	0.61	0.00	11.59	0.61	0.00	0.61	137137
40	2.75	12.77	4.58	35.11	15.27	0.00	4.58	20.61	9.16	6.11	4.58	109542
41	2.80	13.00	9.96	50.96	14.94	0.77	0.00	14.56	3.07	3.07	2.68	327372
42	2.90	14.00	12.50	55.80	10.71	0.89	0.00	12.95	1.79	1.79	3.57	561926
43	3.00	15.00	1.39	54.17	4.86	0.00	0.00	22.92	0.00	8.33	8.33	34404
44	3.10	16.20	6.28	37.17	6.28	0.00	0.00	26.18	2.09	8.38	13.61	191657
45	3.20	17.40	6.42	54.34	6.42	0.00	0.00	13.58	5.66	5.66	7.92	166195
46	3.30	18.60	8.55	42.31	10.26	0.43	0.00	16.67	6.84	8.12	6.84	234805
47	3.35	19.20	4.42	42.54	8.29	0.00	0.00	18.78	4.42	4.42	17.13	181623
48	3.45	20.40	9.30	33.14	9.88	1.16	0.00	16.28	12.79	8.14	9.30	95884
49	3.55	21.65	2.41	48.19	2.41	0.00	0.00	21.69	0.00	18.67	6.63	48991
50	3.70	23.60	7.82	41.56	3.70	0.41	0.00	14.81	5.76	18.52	7.41	110835
52	3.75	24.25	5.59	48.25	1.40	0.00	0.00	16.08	0.00	16.08	12.59	143492
53	3.85	25.55	1.99	26.49	0.66	0.00	0.00	20.53	1.32	37.75	11.26	39874
54	4.00	27.50	0.00	63.64	0.00	0.00	0.00	13.64	0.00	22.73	0.00	787

SI Table 3. RESULTS OF PYROLYSIS ANALYSES (Rock/Eval) of organic-rich sediments from Cuitzeo anomalous zone and black mat from the Clovis site at Murray Springs, Arizona. Analyses were performed at University of Houston Center for Petroleum Geochemistry. Pyrolysis products are expressed as fraction of TOC. Free hydrocarbons are released upon heating to 350 °C and include normal hydrocarbons. Higher hydrogen compounds are generated through thermal cracking of nonvolatile kerogenous organic matter as temperature is increased to 550 °C. Oxygen compounds, measured as CO_2 released at up to 390°C, represent oxygen-bearing organic compounds such as cellulosic plant material. The fraction of reduced molecular carbon is the residue, calculated as one minus the sum of the pyrolysis products.

Sample I.D	%TOC	Free hydrocarbons C<40 (gm HC /gm TOC)	Higher hydrogen compounds (gm HC /gm TOC)	Oxygen compounds (gm CO_2 /gm TOC)	Inert molecular carbon fraction of TOC
Cuitzeo					
2.55m	2.4	0.02	0.12	0.0622	0.8
2.65m	3.7	0.029	0.2	0.068	0.7
2.70m	7.5	0.049	0.45	0.067	0.43
2.75m	15.8	0.016	0.0085	0.025	0.87
2.90m	10.1	0.0023	0.0007	0.02	0.91
Black Mat	2.75	0.008	0.0013	0.054	0.94

SI Table 4. GEOCHEMISTRY of markers using SEM/EDS. Particle #s match images Fig. 5 and SI Fig. 6.

MAGNETIC MICROSPHERULES

Particle #	Diam.	Na2O	MgO	Al2O3	SiO2	SO3	K2O	CaO	TiO2	Cr2O3	MnO	FeO	NiO	P2O5	Rock/Mineral
275 20	50+60	0.000	0.000	0.059	0.425	0.000	0.188	0.385	0.109	0.474	0.207	98.153	0.000	0.000	Magnetite
280 10a	70	0.286	0.190	0.086	0.362	0.738	0.079	0.196	0.131	0.064	0.287	96.779	0.222	0.580	Magnetite
280 10b	25	0.301	0.189	0.109	0.342	0.497	0.116	0.474	0.382	0.053	0.275	96.470	0.233	0.558	Magnetite
280 11	80	0.344	0.200	0.256	1.062	0.633	0.056	0.323	0.109	0.105	0.261	96.023	0.171	0.458	Magnetite
280 12	30	0.163	0.143	0.264	0.807	0.677	0.069	0.338	0.142	0.080	0.366	96.150	0.166	0.636	Magnetite
280 13	100	0.273	0.101	0.196	0.391	1.080	0.224	0.214	0.080	0.031	0.208	96.276	0.114	0.812	Magnetite
280 15	50	0.511	0.184	0.135	0.620	0.649	0.109	0.295	0.077	0.051	0.310	96.301	0.171	0.588	Magnetite
280 2	80	0.322	0.217	0.319	0.517	0.689	0.078	0.369	0.103	0.075	0.212	96.250	0.220	0.629	Magnetite
280 3	45	0.222	0.208	0.031	0.608	0.973	0.061	0.304	0.093	0.070	0.257	96.506	0.160	0.506	Magnetite
AVG:	60	0.269	0.159	0.162	0.570	0.659	0.109	0.322	0.136	0.111	0.265	96.545	0.162	0.530	

FRAMBOIDS

Particle #	Diam.	Na2O	MgO	Al2O3	SiO2	SO3	K2O	CaO	TiO2	Cr2O3	MnO	FeO	NiO	P2O5	Rock/Mineral
275 2	40	0.279	0.398	0.060	1.373	57.670	0.149	0.368	0.159	0.328	0.000	39.216	0.000	0.000	Pyrite
275 5	50	0.910	1.240	1.080	11.912	49.300	0.200	0.960	0.260	0.260	0.020	33.827	0.030	0.000	Pyrite
AVG:		0.594	0.819	0.570	6.643	53.485	0.175	0.664	0.210	0.294	0.010	36.521	0.015	0.000	

GLASSY GRAINS

Particle #	Diam.	Na2O	MgO	Al2O3	SiO2	SO3	K2O	CaO	TiO2	Cr2O3	MnO	FeO	NiO	P2O5	Rock/Mineral
275 4	180	3.85	0.00	24.80	47.97	0.00	0.04	19.78	0.00	0.00	0.00	1.71	1.85	0.00	Tephrite
275 21a	--	2.63	0.06	11.16	61.73	0.69	4.25	5.84	2.58	0.86	0.00	9.85	0.33	0.00	Rhyolite
275 21b	--	1.74	0.71	11.79	70.91	0.89	4.46	2.79	0.95	0.59	0.62	4.55	0.00	0.00	Rhyolite
280 1a	140	1.46	1.49	13.50	64.95	0.00	2.15	3.36	2.63	0.02	0.27	10.05	0.14	0.00	Rhyodacite
280 1b	125	3.39	0.00	12.20	77.89	0.09	5.29	0.54	0.00	0.16	0.00	0.45	0.00	0.00	Alkali rhyolite
280 4	360	3.16	2.15	14.75	59.34	1.06	2.03	5.52	2.50	0.02	0.04	9.34	0.09	0.00	Andesite
280 6	375	2.83	0.38	28.93	46.72	0.65	0.52	18.73	0.63	0.00	0.00	0.60	0.00	0.00	Alkali basalt
280 8	510	5.45	0.00	24.87	56.52	0.06	0.24	10.70	0.00	0.00	0.00	1.68	0.49	0.00	Latite
280 16	180	5.35	0.00	14.42	70.23	0.68	3.54	2.89	0.97	0.00	0.00	1.43	0.50	0.00	Rhyolite
AVG:	267	3.318	0.532	17.379	61.807	0.457	2.503	7.794	1.140	0.183	0.103	4.407	0.376	0.000	

MAGNETIC GRAINS

Particle #	Diam.	Na2O	MgO	Al2O3	SiO2	SO3	K2O	CaO	TiO2	Cr2O3	MnO	FeO	NiO	P2O5	Rock/Mineral
CU2		0.00	0.74	0.42	0.64	0.00	0.00	0.00	37.29	0.00	0.00	60.91	0.00	0.00	Ti-magnetite
CU4		0.00	2.51	0.84	2.25	0.00	0.00	0.00	41.18	0.00	0.00	44.85	0.00	0.00	Ti-magnetite
CUx 500		0.00	0.52	0.00	0.27	0.00	0.00	0.00	44.45	0.00	0.00	50.93	0.00	0.00	Ti-magnetite
CUB2		0.00	0.83	0.00	0.01	0.00	0.00	0.00	42.95	0.00	0.00	52.53	0.00	0.00	Ti-magnetite
CUA		0.00	2.87	0.76	0.50	0.00	0.00	0.00	33.21	0.80	0.00	56.29	0.00	0.00	Ti-magnetite
CU3		0.00	0.00	0.00	0.00	0.00	0.00	0.00	28.87	0.00	0.00	71.13	0.00	0.00	Ti-magnetite
CUB		0.00	0.00	0.00	0.00	0.00	0.00	0.00	28.87	0.00	0.00	71.13	0.00	0.00	Ti-magnetite
CUx 700		0.00	0.36	0.18	0.83	0.00	0.00	0.00	31.70	0.00	0.00	62.73	0.00	0.00	Ti-magnetite
CUA2		0.00	1.70	0.47	1.52	0.00	0.00	0.00	44.40	0.00	0.00	46.60	0.00	0.00	Ti-magnetite
AVG:		0.00	1.06	0.30	0.67	0.00	0.00	0.00	36.99	0.09	0.00	57.45	0.00	0.00	

SI Table 5. MARKER ABUNDANCES by type, depth, and quantity. Notation "n/d" equals "not detected."

Magnetic Spherules (MSp)		Magnetic Grains		Carbon Spherules (CSp)		Nanodiamonds (NDs)		Framboidal Spherules		Charcoal	
meters	#/kg	meters	g/kg	meters	#/kg	meters	ppb	meters	#/kg	meters	#/kg
2.20	114	2.20	2.52	2.20	0	2.20	4	2.20	228	2.20	429
2.25	96	2.25	5.52	2.55	210	2.35	6	2.25	192	2.25	0
2.35	120	2.35	3.00	2.70	156	2.70	10	2.35	480	2.30	0
2.55	126	2.55	0.08	2.75	684	2.75	55	2.55	336	2.35	288
2.65	79	2.65	1.01	2.80	316	2.80	100	2.65	475	2.40	793
2.70	311	2.70	1.20	2.90	n/d	2.90	15	2.70	2333	2.45	1749
2.75	214	2.75	0.77	3.10	n/d	3.10	n/d	2.75	12825	2.50	2831
2.80	2054	2.80	5.75	3.30	n/d	3.60	n/d	2.80	1896	2.55	8028
2.90	216	2.90	15.30	3.40	n/d			2.90	n/d	2.60	2992
3.00	n/d	3.00	5.62	3.50	n/d			3.00	n/d	2.65	76952
3.10	n/d	3.10	8.91	3.60	n/d			3.10	n/d	2.70	23997
3.20	n/d	3.20	6.05					3.20	n/d	2.75	22818
3.30	n/d	3.30	4.09					3.30	n/d	2.80	14886
3.40	n/d	3.40	2.99					3.40	n/d	2.90	8602
3.50	n/d	3.50	6.18					3.50	n/d	3.00	10689
3.60	n/d	3.60	8.30					3.60	85	3.10	28856
										3.20	12780
										3.30	5921
										3.35	6907
										3.45	1196
										3.55	988
AVG:	208		5		124		24		1178		1178

SI Table 6. DATA SOURCES for TERNARY DIAGRAMS of cosmic and impact-related materials plotted in Fig. 6. Materials are shown by type, total # of analyses per type, # of analyses per site, sampling location or type, and references. Notation "cosmic MMs" equals "micrometeorites."

TYPE	TOT#	#SITES	ANAL.	LOCATION or TYPE	REFERENCE
Cosmic spherules	471	3	20	Antarctica	Engrand, 1999
			71	Antarctica	Genge, 1997
			20	Antarctica	Genge, 1998
			14	Antarctica	Rochette, 2008
			279	Antarctica	Taylor, 2002
			14	Antarctica	Rochette, 2008
			45	Atlantic Ocean	Dekov, 2007
			8	Greenland	Maurette, 1986
Cosmic MMs	262	80	21	Antarctica	Engrand, 1999
			86	Antarctica	Genge, 1997
			78	Antarctica	Kurat, 1994
			77	Meteorites	Genge, 1999
TOTAL COSMIC	733	83			
Impact ejecta	30	2	15	KPg	Bauluz, 2004
			12	KPg	Koeberl, 1992
			3	Rio Cuarto	Bland, 2002
Impact spherules	132	3	40	Lonar Crater, IND	Misra, 2009
			79	Nuussuaq, Greenland	Jones, 2005
			13	Tunguska, Russia	Dolgov, 1973
			4	Tunguska, Russia	Glass, 1969
Impact tektites	856	7	6	Australasian tektite field	Amare, 2006
			2	Australasian tektite field	Chalmers,1976
			47	Australasian tektite field	Folco, 2008
			48	Australasian tektite field	Glass, 1990
			47	Australasian tektite field	Glass, 2004
			16	Australasian tektite field	Glass, 2006
			19	Australasian tektite field	Koeberl, 1992
			30	Australasian tektite field	Lee, 2004
			11	Australasian tektite field	Son, 2005
			2	Bahia Blanca, Argentina	Schultz, 2004
			2	Chesapeake Bay crater	Glass, 1990
			28	Chesapeake Bay crater	Glass, 1998
			130	Chesapeake Bay crater	Kelly, 2004
			16	Chesapeake Bay crater	Koeberl, 1998
			7	Chesapeake Bay crater	Koeberl, 2001
			46	Chesapeake Bay crater	Mchugh, 1996
			18	Chesapeake Bay crater	Mchugh, 1998
			7	Chesapeake Bay crater	Povenmire, 1994
			3	Chesapeake Bay crater	Povenmire, 1997
			18	Darwin glass	Koeberl, 1990
			1	Lake Botsumtwi crater	Glass, 1990
			5	Lake Botsumtwi crater	Koeberl, 2006
			194	Lake Botsumtwi crater	Koeberl, 2007
			30	Lake Botsumtwi crater	Leutke, 2008
			1	Ries crater--moldavites	Glass, 1990
			118	Ries crater--moldavites	Trnka, 2002
			4	Zhamanshin crater	Zolensky, 1991
TOTAL IMPACT	1018	12			

SI Table 7. QUANTITATIVE EDS ANALYSIS of ND-rich residue from 2.75-m and 2.8-m strata (averaged). No copper was detected, refuting the speculation about misidentification of copper as YDB diamonds by Daulton *et al.* (2011).

MAJOR ELEMENTS			
Elements (>1%)	Weight %	Atomic %	Error %
C	87.16	96.01	2.43
O	2.49	2.09	0.31
Au (=grid)	6.97	0.52	0.63
Fe	1.10	0.25	0.12
MINOR ELEMENTS w/ high uncertainties			
Elements (<1%)	Weight %	Atomic %	Error %
Al	0.61	0.29	0.07
Ca	0.03	0.01	0.01
Cl (=HCl)	0.07	0.02	0.01
F (=HF)	0.45	0.32	0.03
Ni	0.15	0.03	0.06
Pd	0.03	0.00	0.02
Si	0.92	0.43	0.14
COPPER NOT DETECTED			
Elements	Weight %	Atomic %	Error %
Cu	0.00	0.00	0.00

SI Table 8. D-SPACINGS for four allotropes of nanodiamonds. All measured d-spacings were within 2% of these published values.

Lonsdaleite		Cubic		n-Diamond		i-Carbon	
hkl	d (ang)	hkl	d (ang)	hkl	d (ang)	jkl	d (ang)
100	2.184	111	2.059	111	2.060	110	3.037
002	2.059	220	1.261	200	1.780	111	2.530
101	1.930	311	1.075	220	1.260	200	2.123
102	1.498	400	0.892	311	1.070	211	1.807
110	1.261	331	0.818	222	1.040	220	1.537
103	1.162	422	0.728	400	0.898	311	1.297
200	1.092	511	0.686	331	0.818	400	1.097
112	1.075	333	0.686	420	0.796	422	0.909
201	1.056		0.000	422	0.726	431	0.839
202	0.965			511	0.683		

SUPPORTING INFORMATION—TEXT.

BIOSTRATIGRAPHY-POLLEN. At La Chonta Bog, workers obtained three cores that span the YD: core #1 from Islebe *et al.* (1995) and cores #2 and #CIS from Hodell, *et al.* (2008) (Fig. 2). Percentage data reported for core #1 indicates lowering of the tree line during the YD, resulting in expansion of higher altitude, cold-adapted plant assemblages, along with a contraction of lower altitude plant assemblages. La Chonta #2 core displays percentages and total pollen suggesting a similar expansion during the YD of higher altitude, cold-adapted plant assemblages, as in core #1 (Hooghiemstra *et al.*, 1992). This core exhibits six zones in which no pollen grains were found, and one of those coincided with the La Chonta stadial, which these authors correlated with the YD (used to plot Fig. 2). These authors did not address whether the absence of pollen resulted from lack of preservation, low productivity, or other reasons; however, it appears that the absence zones are related to cooler climate since all six occur only during the Late Glacial and YD episodes. The third core (CIS-La Chonta) was not dated but was cross-correlated with other cores such that the pollen records of all three cores display the effects of the YD climate change and are similar to Lake Cuitzeo record.

EELS ANALYSES. For this analysis, electrons undergo inelastic scattering with energy losses that are element-specific. For carbon, an EELS spectrum will display two main peaks, a pi* peak at about 282 to 285 eV and a sigma* peak at about 295 to 300 eV. Neither peak will appear if the material being analyzed with EELS lacks carbon. The pi* peak is an indicator of the presence of sp^2 bonding, meaning that a given carbon atom is bonded to three neighboring carbon atoms, while the sigma* peak indicates more complex bonding to four neighbors. Graphite displays only lower-order sp^2 bonds, while cubic NDs displays only higher-order sp^3 bonding. Other carbonaceous materials, such as amorphous carbon, display a mix of sp^2 and sp^3 bonding (Orwa and Peng 2001, Dadsetani 2010), as do n-diamond and i-carbon. N-diamond displays about 95% sp^3 higher-order bonding, and i-carbon has about 95% sp^2 lower-order bonding, but only 5% sp^3 (Peng 2001). EELS performed on the Lake Cuitzeo nanoparticles produced the spectrum shown in Fig. 9, which reveals a subdued pi* peak at about 285 to 287 eV. This indicates less sp^2 lower-order bonding than found in amorphous carbon or graphite. The pi* peak for Lake Cuitzeo is similar to all the other curves from independent researchers for n-diamonds and i-carbon, as shown in Fig. 9 (Santiago, 2004; Yang, 2008; Konyashin, 2006; Kurbatov, 2010; Peng, 2001). This indicates that the observed nanoparticles for Lake Cuitzeo also are n-diamonds and i-carbon. Also, the pi* peak is an indicator of sp^2 bonding, which would not be present in cubic NDs or lonsdaleite. Its presence in the spectrum results from at least two possible causes. First, it may be visible because n-diamond and i-carbon contain a mix of sp^3 and sp^2 bonding, and the latter will contribute to the pi* peak. Second, the pi* peak may result from the presence of amorphous carbon or graphite, because the NDs are mostly observed inside carbon onions or surrounded by amorphous carbon, which has sp^2 bonding that would contribute to the pi* peak. This has been observed previously in diamonds found in meteorites, where the nanoparticles appear to be coated with graphite or amorphous carbon. Both the sigma* and pi* peaks appear to be about 2 to 5 eV higher than for amorphous carbon, i.e., "blue-shifted," which is typical of n-diamonds (Dadsetani 2010).

EFTEM ANALYSIS. We created two maps of a region of nanoparticles. For the first, we acquired an EELS "zero-loss" image of the region and detected the presence of multiple crystals displaying lattice fringes

(Fig. 10A, lighter particles 1 through 4). FFTs and lattice measurements confirmed that the nanoparticles are consistent with being NDs allotropes. Second, we generated a map of energies around 299 eV, known as a "jump ratio," that records the sigma* peak of carbon, if present, and compares it against the background energies. To simplify the comparison to the jump ratio in Fig. 10, we inverted the zero-loss image to create a negative. The results indicate that the lighter areas (particles 1 through 4) contain substantial amounts of sp^3 bonding (Fig. 10A). Those enhanced-sp^3 areas correspond very well with the lighter crystalline nanoparticles visible in the inverted zero-loss image (Fig. 10B). The area near particle 3 exhibits amorphous carbon film (from the TEM grid) with almost no residue on top. This region appears dark, which is consistent with the lack of sp^3 bonding.

SUROVELL *et al.* (2009). Those authors claimed to have closely followed the Firestone *et al.* protocol (2007a, 2007b) for quantification of MSp. LeCompte *et al.* (2011) compared their protocol with that of Firestone *et al.*, and this comparison revealed that the methods of Surovell *et al.* differed substantially in several critical ways, as described below. For two sites common to both studies, Surovell did not observe a single MSp in the YDB and, therefore, claimed to refute the results of Firestone *et al.* However, LeCompte *et al.*, an independent group, retested those two sites and reported MSp values ranging from ~100 to >1000 MSp/kg, confirming the results of Firestone *et al.* and refuting the results of Surovell *et al.* They concluded that the changes in protocol introduced by Surovell *et al.* led to fatal flaws in their extraction, identification, and quantification of YDB MSp, all of which invalidate that group's conclusions, as follows:

Deficiency #1: YDB Samples Too Thick Stratigraphically. A) Quote from Firestone *et al.* (2007a) regarding the YDB interval: *"we found a thin, sedimentary layer (usually <5 cm)."* **B)** Source, Table S1 in Surovell *et al.* (2009) shows that the candidate YDB interval at 7 sites was sampled at a resolution ranging from 5-28 cm, averaging 11 cm. **Problem:** Firestone *et al.* collected sediment samples at 7 sites at which they discovered high abundances of YDB markers in a thin layer with vertical thicknesses ranging from 0.5 to 5 cm and averaging 2.3 cm, as illustrated in their Fig. 1 in Firestone *et al.* Surovell *et al.* collected some samples that were sufficiently thin, but also collected much thicker samples, ranging up to 28 cm thick (averaging 11 cm), much wider than the average YDB layer averaging 2.3 cm where the MSp are concentrated. The thickest sample (28 cm) collected by Surovell *et al.* diluted the markers by an average of ~5× and up to ~60×, masking. Although we do not consider this to be a fatal deficiency, it does make spherule detection more difficult.

Deficiency #2; Inadequate Aliquot Size. A) Quote from Firestone Protocol (2007b), who analyzed *"one or more ~100-200 mg aliquots….Microspherules are usually rare, often making it necessary to inspect the entire magnetic fraction."* **B)** Quote from Surovell *et al.* (2009): they *"examined 10–40 mg … per sample,"* and never examined the entire magnetic fraction. **Problem:** This deficiency means that Surovell *et al.* examined up to 20× fewer magnetic grains than Firestone *et al.*, further reducing the resolution necessary to find the MSp.

Deficiency #3: Size-Sorting. A) Quote from Firestone Protocol (2007b): *"We used ASTM sieves to screen the magnetic grains into separate fractions and worked mostly with the <150-µm samples."* **B)** Source, Surovell *et al.* (2009): They utilized only a "1-mm sieve." **Problem:** Adequate size-sorting is essential in order to overcome the difficulty in detecting rare MSp among other, more abundant magnetic grains. Also, during normal handling of the magnetic fraction, the grains tend to separate by size, meaning that the fine grains tend

to move to the bottom of the container. Hence, drawing test samples from the upper layers results in preferential selection of coarser detrital magnetic grains, potentially missing the smaller MSp that become concentrated in the finer material beneath. Failure to size-sort represents a fatal flaw in their analyses. Furthermore, in those instances where the entire sample is not examined, it is critically important to work with well-mixed representative aliquots to assure an even distribution of MSp. A mechanical sample splitter is the preferred instrument for splitting the magnetic fraction, although careful manual splitting will suffice.

Deficiency #4: Perfect Sphericity. A) Source, Fig. 2 in Firestone *et al.* (2007a): two of the four MSp shown in Fig. 2 are highly spherical, but the other two are not. **B)** Quote from Surovell *et al.* (2009): they elected to *"eliminate a number of particles that at first glance appeared to be highly spherical but were not."* **Problem:** The approach of Surovell *et al.* differed from that of Firestone *et al.* by only counting those candidate spherules with a high degree of sphericity, even though it is well recognized that cosmic and impact microspherules often are non-spherical (Taylor, 2000, 2002). Such non-spherical objects occur frequently in Lake Cuitzeo, where such an overly rigorous protocol would have meant not counting the MSp shown in Figs. 5D, 5F, SI Figs. 6A, 6C, and 6D, resulting in an undercount in YDB MSp by ~50%.

Deficiency #5: No SEM/EDS Analyses. A) Quote from Firestone Protocol (2007b): *"Selected microspherules were mounted, sectioned, and analyzed by XRF [SEM-EDS] and/or laser ablation."* **B)** Source, Surovell *et al.* (2009): no MSp were reported to have been analyzed. **Problem:** Firestone *et al.* analyzed MSp using SEM-EDS, as in the present study. Both investigations indicate that the observed YDB MSp are not of anthropogenic, volcanic, or cosmic origin, but instead match quench-textured spherules from known impact events. Furthermore, while detrital magnetic grains and framboidal spherules may appear to be MSp under a light microscope, examination by SEM/EDS can show that they are not. The Surovell *et al.* group did not conduct any SEM analyses, resulting in potentially counting apparent spherules that were not impact-produced, and thereby leading to erroneous values, especially outside the YDB. In our experience, most candidate "spherules" outside the YDB tend to be detrital grains or framboidal spherules, rather than true MSp. Regarding this, Pinter *et al.* (2011) did not to recognize the difference between quench-melted MSp as compared to rounded detrital grains and framboidal spherules, which are readily differentiated using SEM/EDS.

CARBON ONIONS. These particles are nm-sized, multi-shelled, and fullerene-like. Space telescopes have detected far ultraviolet (UV) signals interpreted to result from the presence of carbon onions containing NDs that formed in the explosions of distant stars (Yastrebov 2009). Onions have also been observed in meteorites (Smith, 1981) and interstellar dust particles, or IDPs (Rietmeijer, 1997). In the laboratory, NDs have been created inside carbon onions by various methods such as: 1) during TNT detonation using low-oxygen, high-carbon explosives (Kuznetsov 1994); 2) after exposure to electron irradiation at 700°C in a vacuum (Banhart, 1997), in one case, forming star-twins (Huang, 2007) that appear identical to those found in the YDB (Fig. 11A); 3) after exposure to MeV ion irradiation at 700 to 1000°C (Weslowski, 1997); 4) after heating to about 600°C in pure oxygen with a laser beam (Yoshimoto, 1999); and 5) after heating commercial NDs to 1700°C in argon to form carbon onions, and then reheating the onions to 500°C in air to induce reversion to NDs (Tomita, 2000). None of these laboratory processes are duplicated in nature, since all require unusual

energy sources, e.g., lasers or ion beams, and/or exotic atmospheres, e.g., argon or a vacuum.

Carbon onions occur in commercial wood charcoal that has been heated to 700°C in an atmosphere of argon (Hata 2000), but are not reported to contain NDs. Onions have also been detected in natural wildfires (Cohen-Ofri, 2001), but no NDs were observed in those onions. To test the wildfire hypothesis, we analyzed charcoal and CSp from a modern intense crown fire that had been previously examined (Firestone, 2007). We detected carbon onions (SI Fig. 11B), but neither the onions nor CSp contained NDs. Previously, Kimbel *et al.* (2008) reported simulating wildfires under laboratory conditions at about 500°C in order to create CSp from burned pine resin. Those CSp appear identical to the ones found at Lake Cuitzeo and other YDB sites, but are dissimilar to fungal sclerotia published by Scott *et al.* (2010).

Kimbel *et al.* (2008) reheated the CSp to about 1000°C under hypoxic conditions (steam or argon), which produced NDs inside the CSp. This novel process of nanodiamond formation is patent-pending in 42 countries. Using the TEM, we analyzed some of the reheated CSp and detected large carbon onions and NDs inside the CSp (SI Fig. 11A), but the NDs were only observed outside the onions. It appears that simultaneous production of both onions and NDs requires three primary conditions: a) a high-carbon feedstock (pine resin, in this case); b) temperature in excess of 1000°C and c) hypoxic conditions of <3% oxygen, which is necessary to suppress diamond combustion above 600°C. Hypoxia was a requirement for diamond production in that experiment, but such low oxygen levels (<3%) do not occur in wildfires, since those levels preclude either flaming or smoldering fires, and by definition, a wildfire could not occur (Miller, 2001). There is no evidence that carbon onions containing NDs can form in forest fires.

CVD (CARBON VAPOR DEPOSITION). For typical CVD in the laboratory, a substrate is used to condense carbon from one or more carbon-rich precursors, such as methane, producing cubic NDs, n-diamonds, i-carbon, and lonsdaleite (Wen, 2006; Maruyama 1992). For example, although CVD NDs can form under low pressure and moderate temperatures of 450°C to 1200°C (Daulton, 1996), they do so only within an inert atmosphere, since NDs combust under oxidizing conditions. There is no evidence that conditions necessary to produce NDs by CVD can be duplicated inside forest fires, volcanic eruptions, or by any other natural terrestrial mechanism. The $\delta^{13}C$ values reported by the Tian group are not meteoritic but do not preclude impacts or airbursts that created CVD-like NDs from terrestrial material.

METHODS.

PROTOCOL: Anomalous Zone (2-4 M). Samples, approximately 2 cm-thick were taken every 5 cm. In addition to the reconnaissance analyses summarized above, anomalous zone organic matter was analyzed by scanning electron microscopy (SEM), pyrolysis chromatography (Rock/Eval, University of Houston) and gas chromatograph-mass spectroscopy (GC-MS) of the solvent-extractable organic fraction at the U.S. Geological Survey. Isolation and identification of charcoal, pollen and diatoms, and analyses for %TIC and %TOC were carried out at the Geology Department of the Instituto de Metalurgia, Universidad Michoacana de San Nicolás de Hidalgo in Morelia. Complete results are given in Israde *et al.* (2010).

Charcoal particles were isolated from sediment samples after treatment with strong solutions of potassium hydroxide and hydrogen peroxide, wet sieving (125μm), and observation under a binocular microscope. Charcoal appears as angular, black (opaque) particles. AMS radiocarbon analyses were

15

performed on bulk organic matter from 19 samples taken in the uppermost 10 m chosen for their high %TOC content. Dating uncertainties ranged from ±50 to ±2885. Samples were processed using standard procedures and targets were prepared at USGS laboratory in Reston, Virginia and analyzed at Lawrence Livermore National Laboratory AMS facility and also at the University of Arizona AMS facility.

 PROTOCOL: Nanodiamonds (NDs). Disaggregated and sieved bulk sediments were digested initially with hydrochloric acid to remove soluble organic compounds and carbonates. Digested residues were then oxidized with acidic dichromate solution at elevated temperatures to remove insoluble organic contaminants and any residual carbonates. NDs were next extracted from the digested residue using aqueous sodium hydroxide solution. The alkaline colloidal NDs extractions were then acidified using hydrochloric acid to below a pH of 1 and kept at elevated temperature for several days allowing the NDs to flocculate. Next, the extracted residues were treated with a solution of hydrofluoric and hydrochloric acids with ultrasonication to remove silicates. Extracted residues were then oxidized again using acidic dichromate until all residues appeared colorless. All remaining residue solids were then rinsed under acidic conditions and dried before being massed. The extraction process yielded a carbon-rich acid-resistant residue that is a heterogeneous mixture of carbon nanocrystalline particles mixed with amorphous carbon, along with residual amounts of minerals such as quartz. There are inherent difficulties and uncertainties in manipulating and identifying objects approaching 1 nm, and also the presence of large amounts of amorphous carbon makes the NDs more difficult to identify. The reported abundances for NDs are estimates (about ±50%), due to the difficulties of quantifying nanogram-sized batches with the TEM.

 After processing, small samples were deposited by pipette onto carbon-coated transmission electron microscope (TEM) grids composed of gold or molybdenum, depending upon the analytical method being used. We avoided using copper grids due to possible of confusing copper diffraction patterns with those of NDs. For NDs identification, standard techniques were used for HRTEM, STEM, SAD, FFT, EDS, EELS, and EFTEM.

 PROTOCOL: Magnetic Spherules and Grains, specific to Lake Cuitzeo. To test for the presence of the sedimentary markers reported by previous researchers, we took sediment samples ranging in weight from about 5 to 20 grams. Because these were from a small-diameter lake core, samples were smaller than the sediment samples of up to 500 grams typically utilized by Firestone *et al.* (2007) The samples were discontinuous with each sample representing about 1-cm thickness out of a total sample thickness that varied from 5 to 10 cm. The grains were isolated using a grade-42 neodymium magnet, extracted from sediment slurry made from each sample. The grains were screened into various size groups from >150 μm to >53 μm, after which the particles were extracted and counted by hand-picking using a 300-power, reflected-light microscope. The magnetic fractions were small, so we viewed all particles in both fractions. Selected MSp, glassy grains, and magnetic grains (titanomagnetite) were affixed to SEM tabs attached to either SEM stubs or glass slides, and then, analyzed by SEM-EDS. Carbon particles were separated from the sediment slurry by flotation and hand-picking, after which they were also affixed to SEM stubs or slides and analyzed, as described below.

PROTOCOL: Magnetic and Carbon Markers, General (Version 2011-06-10).

Extraction from Sediment. Mostly, we separated magnetic grains manually, but automated processing can be accomplished with, for example, a Franz magnetic separator. We avoided sonication with a ceramic magnet because that process typically collects only strongly magnetic grains and excludes the smallest MSp. We used only **grade-42 or grade-52 neodymium magnets.** All other magnets are too weak to extract enough magnetic grains. Typically, we used the size 2"×1"×0.5", which was convenient for both field and laboratory work. One source for these is K&J Magnetics, (http://www.kjmagnetics.com/), item # BY0X08-N52. **CAUTION: These powerful magnets can be dangerous. Keep them well away from metal objects, which they strongly attract. Also, their magnetic fields can damage credit cards, motel card keys, and electronic devices.**

Extracting the magnetic fraction (Fig. A) from all types of sediment.
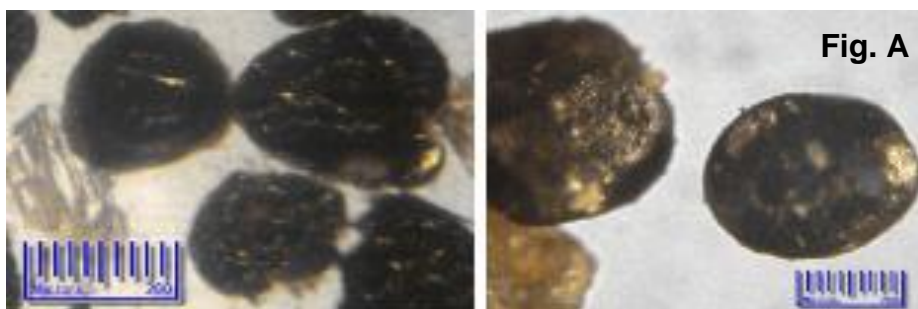
Fig. A. Magnetic Grains

- Outlying sediment samples either older or younger than the Younger Dryas Boundary layer (YDB) often were sampled at thicknesses of 5 cm to 20 cm. For the YDB, we collected bulk sediment samples at typical thicknesses of about **0.5 cm to 2 cm** and at weights of **at least 500-1000 grams. CAUTION: smaller weights and thicker YDB sections may be insufficient for detecting peaks in markers.**

- Bulk samples were thoroughly mixed to homogenize the sediment and were then dried at room temperature. Last, they were weighed. All processing was done with non-metallic tools to avoid introducing foreign metals, and care was taken not to crush the carbon fraction.

- The magnet was placed into a durable 4-mil plastic bag to prevent grains from sticking to the magnet (Fig. B). Thicker supermarket freezer bags are also adequate for this purpose. Next, we added adequate water to each sediment sample to create a slurry (Fig. C).

17

- We usually processed **~500** to **1000 grams for each stratum** in multiple batches. However, if a sample has abundant magnetic grains (for example, more than 1 gram/kg), you may need to use only aliquots of 150-500 grams.

- The magnet, tightly stretched in the bag, was immersed in the mixture (Fig. D). **NOTE: The magnet should be moved slowly and gently, otherwise water action will dislodge the smaller grains.**

- The magnetic fraction (at arrow, Fig. E) was withdrawn along with the bag and magnet.

Fig. D

Fig. E

- The bag, magnet, and grains were then immersed in a second container of clean water. The grains were released from the magnet into the water by withdrawing the magnet from the bag (Fig. F).

- The above were repeated (~15-20×) until minimal additional grains could be extracted (~15-30 min).

- Excess sediment often is extracted along with the magnetic fraction, and so to remove it, the bag and magnet were used to retrieve the magnetic fraction from the second container (arrow, Fig. G). If the water is very dirty, it may be necessary to repeat the process with a third container containing clear water in order to further rinse the extracted magnetic grains. **This process is essential in order to clean the magnetic fraction well enough to visually detect the MSp.**

Fig. F

Fig. G

- After removing the magnet, the wet grains stuck to the bag and could be transferred to a lab dish by touching the bag to a small amount of water on the dish surface (Fig. H). After removing as many as

possible, pour the remaining water slowly over the magnet to extract the remaining grains.

- After drying, the magnetic fraction was weighed and catalogued. The dried fraction appears as below (Fig. I).

- The magnetic fraction was analyzed by SEM/EDS, PGAA, INAA, and/or ICP-MS for ~50 elements, including iridium, thorium, uranium, chromium, and nickel.

Fig. H

Plastic Bag

Fig. I

4 cm

Extraction of Magnetic Spherules (MSp).

- The magnetic fraction was extracted as described above. MSp range from 2 to 150-um in size, and are frequently rounded or oblong, rather than spherulitic (range of shapes shown in Fig. J). Also, not all will be highly polished and reflective. Typically, they will be recognizably different from the terrestrial magnetite, but some judgment is required in selecting candidates. SEM analysis can provide definitive identification of rapid-quench textures.

Fig. J
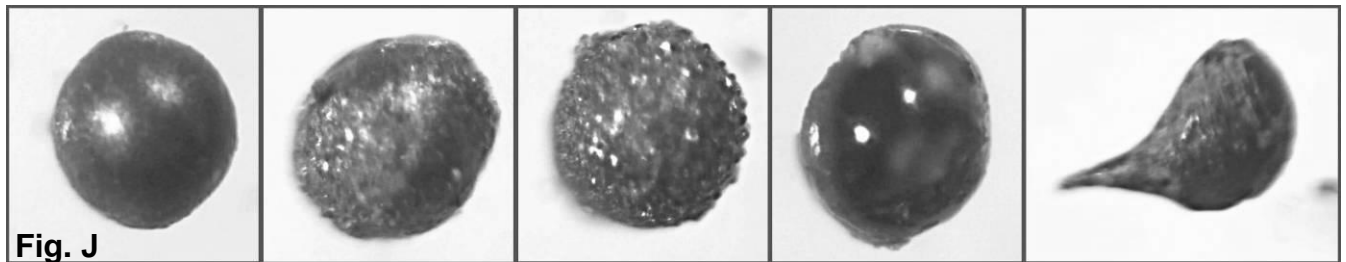
- We used ASTM sieves to screen the grains into three typical fractions: >150 um (ASTM #100 screen), <150 um to >53 um (ASTM #270 screen), and <53 um. Sometimes, we used an ASTM #400 screen to further separate the grains to <38-um. The smallest samples of <53 um or <38-um typically contained the most abundant MSp. **CAUTION: Size separation is essential, since the magnetic grains undergo sorting by size inside a vial, causing most of the small MSp to settle to the bottom (fining downward). If researchers then extract a test aliquot from the upper spherule-depleted layers of the vial, this can produce a serious undercount. For a large multi-gram magnetic fraction, it may be necessary to use a microsplitter, in order to assure even splitting of grains.**

- One or more ~100-200 mg aliquots of the separate magnetic fractions were separated and weighed. MSp are rare, often making it necessary to inspect the entire magnetic fraction from **500-1000 grams** of

sediment. Sometimes, there were only 6 MSp per 1000 grams of sediment, and yet, this amount was above background. **CAUTION: If only 0-2 MSp are detected, it is necessary to analyze additional aliquots in order to obtain an accurate count up to the entire magnetic fraction from 1 kg.**

- To find MSp, we dusted the magnetic grains lightly across a sample tray or microscope slide or at about **10-20 mg per slide** (Fig. K), being careful to **avoid leaving dense clusters of grains**, which made it difficult to distinguish the MSp. A white background makes it easier to locate the MSp. As an alternate to the slide, a lab dish with low sides can be used, so the material does not roll off.

- We scanned using a **reflected-light (top-lit) zoom microscope** with a mechanical stage **at a magnification of not less than 200× up to 300×.** At lower resolution, the MSp may be easily overlooked. Generally, an adequate search for MSp from each individual bulk sample took a total of about 1 to 3 hours, varying by size of the magnetic fraction and number of MSp in the fraction.

- The MSp were tallied and photographed at a magnification of ~300× to 500×. Abundances were extrapolated to determine number of MSp per kg of bulk sediment.

- Selected MSp were removed manually using a sharpened, moistened, wooden probe, or a fine-tipped bristle brush. They were placed either inside a conical-bottom vial filled with alcohol or onto a microprobe/SEM adhesive tab. Selected MSp were sectioned and/or analyzed by SEM-EDS. Typical MSp display dendritic quench-melt texturing (Fig. L).

SPHERULE SUMMARY. Identifying the MSp can be very difficult because many are <40 microns in diameter. To increase the chance of success, here is a summary of the most important points:

1) Homogenize the dried bulk sediment before removing an aliquot of sediment.
2) Use a grade-42 or grade-52 neodymium magnet to extract the magnetic fraction.
3) Be prepared to extract the magnetic fraction from up to 500-1000 grams of sediment.
4) Sieve the extracted magnetic grains by size. Begin work with the >53-um or >38-um fraction.
5) Spread the magnetic fraction evenly across a sample tray or white microscope slide.
6) Use a reflected light (top-lit) zoom microscope with a mechanical stage at not less than 200×.
7) Stop after having found >5-10 MSp, which may mean analyzing the entire magnetic fraction.
8) Use SEM/EDS to search for evidence of dendritic quench-melt crystallization.

Fig. K

2 cm

Fig. L
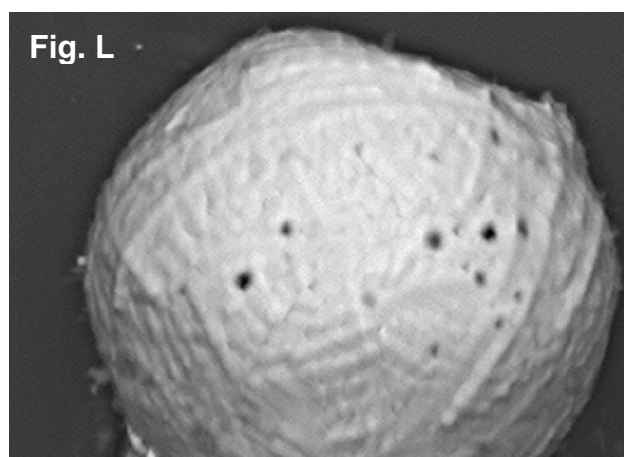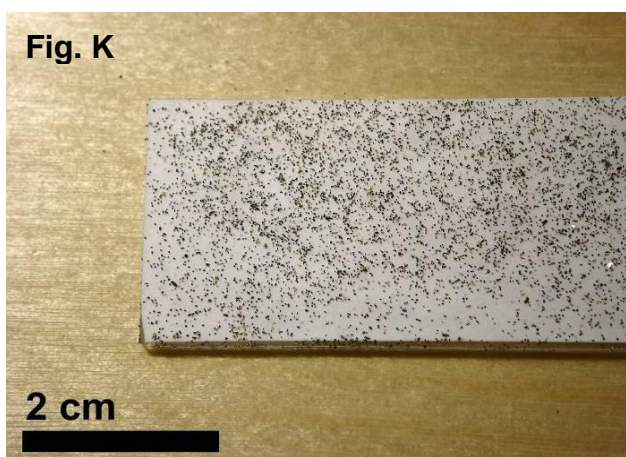
PROTOCOL: Extraction of Carbon Spherules (CSp), Glass-like Carbon, and Charcoal.
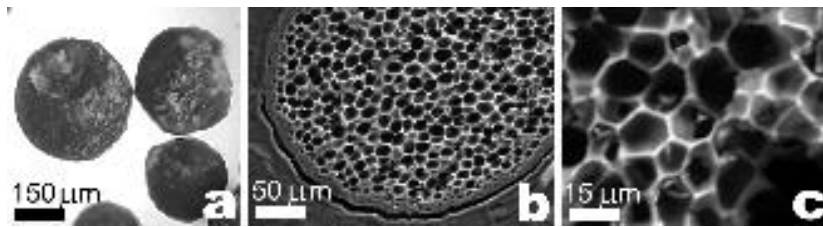
Fig. M. Carbon spherules.
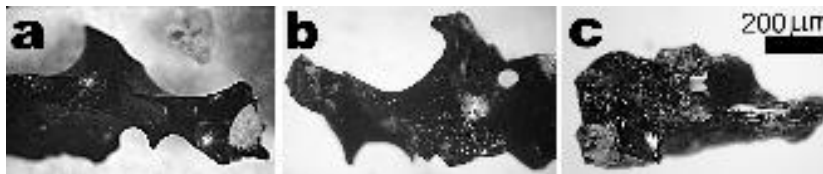
Fig. N. Glass-like carbon.

- Since CSp and glass-like carbon (Figs. M-N) generally are less dense than water, floatation was used for separation. Ample water was added, and the slurry was agitated to free the floating fraction (arrows, Fig O).
- Use an ASTM #200 screen to remove the floating fraction. Since some CSp will pass through a screen, the remainder were skimmed off manually and placed onto a lab dish to dry (Fig. P).
- This was repeated until the entire floating fraction was removed.
- Then, to recover the less buoyant fraction of carbon that did not float, the remaining slurry was agitated and rinsed repeatedly. This stratified the sediment and brought the remaining non-floating carbon fraction to the surface of the sediment sample, but still beneath the water. Any visible carbon, which included charcoal and glass-like carbon, was poured off and separated manually.
- The sample was then dried at room temperature, so as not to destroy the carbon.
- The CSp were separated in two steps. First, they were collected gravimetrically by agitating the dried sample on a smooth, inclined surface, down which they roll easily. Second, the residue was spread on a slide and viewed with an optical microscope (Fig. Q). In order to see CSp down to 10 micron in diameter, it is necessary to use a reflected-light (top-lit) zoom microscope at a **magnification of 180× to 300×. At lower resolution, the CSp can be easily overlooked.**


Fig. O

Fig. P

- Glass-like carbon and charcoal, contained in the same sample, were identified visually and extracted manually, using a thin, sharpened, moistened, wooden probe.
- All three types of carbon were weighed separately, and abundances were calculated in #/kg for CSp or g/kg for charcoal and glass-like carbon.
- CSp and glass-like carbon were tested using various analytical methods, including SEM-EDS, PGAA, INAA, and MS-ICP.
- About 1-10% of the CSp contain NDs, along with only a few pieces of glass-like carbon. Thus, it is essential to analyze 15-20 CSp at the same time in order to detect NDs with STEM and/or TEM, as described in a separate protocol. They were confirmed using selected area electron diffraction (SAD), electron *energy loss* spectroscopy (EELS), and high-resolution electron microscopy (HRTEM).

Fig. Q

1 cm
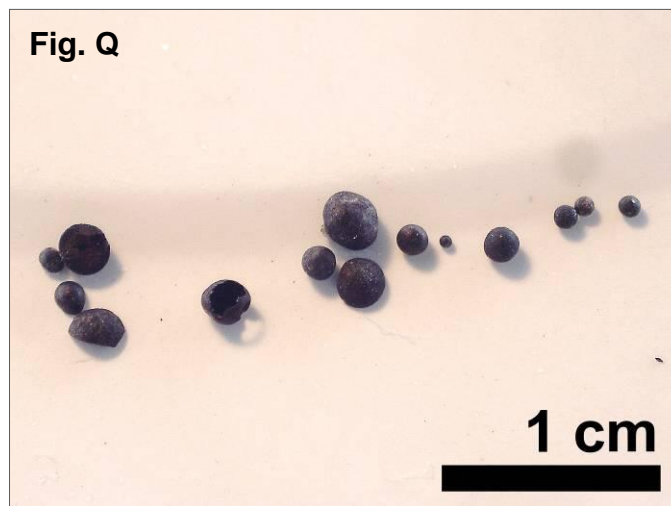
PROTOCOL: Extraction of Aciniform Soot.

As described in Wolbach *et al*. (1985, 1990), we used multiple acids and bases in a standard protocol to extract carbon from bulk sediment. The resulting carbon-rich acid-resistant residue concentrates were then inspected with SEM imaging to search for aciniform soot.

For questions about extraction of aciniform soot and nanodiamonds, email: Wendy Wolbach (mailto:wendywolbach@gmail.com**).**
For questions about magnetic spherules and all other proxies, contact: Allen West (mailto:allen7633@aol.com**).**

SUPPLEMENT REFERENCES

Amare K, Koeberl C (2006) Variation of chemical composition in Australasian tektites from different localities in Vietnam. Meteoritics & Planetary Science 41, Nr 1, 107–123.

Banhart F (1997) The transformation of graphitic onions to diamond under electron irradiation. J. Appl. Phys. v. 81 (8), p. 3440-3445.

Bauluz B, Peacor DR, Hollis CJ (2004) TEM study of meteorite impact glass at New Zealand Cretaceous-Tertiary sites: evidence for multiple impacts or differentiation during global circulation? Earth and Planetary Science Letters 219, 209-219.

Bland PA, *et al.* (2002) A Possible Tektite Strewn Field in the Argentinian Pampa. Science 296, 1109.

Burkhard G, *et al.* (1994) Carbon phase transition by dynamic shock compression of a copper/graphite powder mixture. Jpn J Appl Phys 33:L876–L879.

Bush MB, *et al.* (1992) A 14,300-Yr Paleoecological Profile of a Lowland Tropical Lake in Panama. Ecological Monographs 62:251–275.

Carlisle BC, Braman RB. (1991) Nanometre-size diamonds in the CretaceouslTertiary boundary clay of Alberta. Nature, v. 352, p. 708–709 (1991).

Chalmers RO, Henderson EP, Mason B (1976) Occurrence, Distribution, and Age of Australian Tektites. Smithsonian Contributions To The Earth Sciences, Number 17.

Correa-Metrio, A. (2010) Climate and vegetation of the Yucatan Peninsula during the Late Pleistocene. Florida Institute of Technology. PhD dissertation, Melbourne FL. 194 pp.

Dadsetani M, Titantah JT, Lamoen D (2010) Ab initio calculation of the energy-loss near-edge structure of some carbon allotropes: Comparison with n-diamond. Diam Relat Mater 19:73–77.

Daulton T, Pinter N, Scott A (2010) "No evidence of nanodiamonds in Younger-Dryas sediments to support an impact event". PNAS 107 (37): 16043–16047.

Dekov VM, *et al.* (2007) Cosmic spherules from metalliferous sediments:A long journey to the seafloor. N. Jb. Miner. Abh., Vol.183/3, p. 269–282.

Engrand C, Deloule E, Robert F, Maurette M, Kurat G (1999) Extraterrestrial water in micrometeorites and cosmic spherules from Antarctica: An ion microprobe study. Meteoritics & Planetary Science 34, 773-786.

Firestone RB, *et al.* (2007a) Evidence for an extraterrestrial impact 12,900 years ago that contributed to the megafaunal extinctions and the Younger Dryas cooling. Proc Natl Acad Sci USA 104:16016–16021.

Firestone RB, *et al.* (2007b). Separation of YD Event Markers (8/10/2007).

Folco L, *et al.* (2008) Microtektites from Victoria Land Transantarctic Mountains. Geology, Vol. 36, No. 4, pp. 291-294.

Galindo De Obarrio M (2005) Water quality and its spatial variability in lake Cuitzeo, Mexico. Enschede, ITC.

Genge M, Grady M (1998) Melted micrometeorites from Antarctic ice with evidence for the separation of immiscible Fe-Ni-S liquids during entry heating. Meteoritics &Planetary Science 33, 425-434.

Genge M, Grady M. (1999) The fusion crusts of stony meteorites: Implications for the atmospheric reprocessing of extraterrestrial materials. Meteoritics & Planetary Science 34, 341-356.

Genge MJ, Grady M, Hutchison R. (1997) The textures and compositions of fine-grained Antarctic micrometeorites: Implications for comparisons with meteorites. Geochimica et Cosmochimica Acta, Vol. 61, No. 23, pp. 5149-5162.

Gilmour I, *et al.* (2003) Geochemistry of carbonaceous impactites from the Gardnos impact structure, Norway. Geochimica et Cosmochimica Acta 67:3889{3903.

Gilmour I, French BM, Franchi IA, Abbott JI, Hough RM, Newton J, Koeberl C (2003) Geochemistry of carbonaceous impactites from the Gardnos impact structure, Norway, Geochimica Acta, Vol 67. No. 20. P 3889 - 3903.

Glass BP, Koeberl C (2006) Australasian microtektites and associated impact ejecta in the South China Sea and the Middle Pleistocene supereruption of Toba. Meteoritics & Planetary Science 41, Nr 2, 305–326.

Glass BP (1990) Tektites and microtektites: key facts and inferences. In: L.O. Nicolaysen and W.U. Reimold (Editors), Cryptoexplosions and Catastrophes in the Geological Record, with a Special Focus on the Vredefort Structure. 171: 393-404.

Glass BP, Koeberl C (1999) Ocean Drilling Project Hole 689B spherules and upper Eocene microtektites and clinopyroxene-bearing spherule strewn fileds. Meteoritics & Planetary Science 34, 197-208.

Glass BP, Huber H, Koeberl C (2004) Geochemistry of Cenozoic microtektites and clinopyroxene-bearing spherules. Geochimica et Cosmochimica Acta 69, 3971-4006.

Grieve RAF, Masaitis VL (1994) The economic potential of terrestrial impact craters. international Geology Review 36: 105-151

Gurov EP, Koeberl C, Reimold WU, Brandstätter F, Amare, K (2005) Shock metamorphism of siliceous volcanic rocks of the El'gygytgyn impact crater (Chukotka, Russia). GSA Special Paper 384.

Gurov EP, Koeberl C, Reimold WU, Brandstätter F, Amare K (2005) Shock metamorphism of siliceous volcanic rocks of the El'gygytgyn impact crater (Chukotka, Russia). GSA Special Paper 384.

Hata T, Imamura Y, Kobayashi E, Yamane K, Kikuchi K (2000) Onion-like graphitic particles observed in wood charcoal. J Wood Sci 46:89–92. 22.

Haynes, CV Jr. (2007) Appendix B: Nature and Origin of the Black Mat, Stratum F2, In: Haynes, C. V., Jr. and Huckell, B. B. (Eds.) Murray Springs: A Clovis Site with Multiple Activity Areas in the San Pedro Valley, Arizona. University of Arizona Press, Tucson, AZ, pp. 240-249.

Heymann D, Cataldo F, Pontier-Johnson M, Rietmeijer F (2006) Fullerenes and Related Structural Forms of Carbon in Chondritic Meteorites and the Moon in Natural Fullerenes and Related Structures of Elemental Carbon. Developments in Fullerene Science, 2006, Volume 6, 145-189.

Hough RM, Gilmour I, Pillinger CT, Langenhorst F, Montanari A (1997) Diamonds from the iridium-rich K-T boundary layer at Arroyo el Mimbral, Tamaulipas, Mexico. Geology, vol. 25, Issue 11, p.1019-1022.

Huang JY (2007) In Situ Observation of Quasimelting of Diamond and Reversible Graphite Diamond Phase Transformations. Nano Letters, vol. 7, issue 8, pp. 2335-2340.

Israde-Alcántara I, Velázquez-Durán R, Lozano García MS, Bischoff J, Domínguez Vázquez G, Garduño Monroy VH (2010) Evolución Paleolimnológica del Lago Cuitzeo, Michoacán durante el Pleistoceno-Holoceno, *Boletín de la Sociedad Geológica Mexicana* Vol. 62, núm. 3, p. 345-357.

Kleiman J, Heimann RB, Hawken D, Salansky NM (1984) Shock compression and Flash heating of graphite/metal mixtures at temperatures up to 3200 K and pressures up to 25 GPa. Journal of Applied Physics, Volume 56, Issue 5, September 1, 1984, pp.1440-1454.

Koeberl C, Kruger FJ, Poag CW (2001) Geochemistry of surficial sediments near the Chesapeake Bay impact structure and the search for source rocks of the North American Tektites. Lunar and Planetary Science XXXII.

Koeberl C (1992) Geochemistry and origin of Muong Nong-type tektites. Geochimica et Cosmochimica Acta 56, 1033-1064.

Koeberl C (1998) Identification of meteoritical components in impactites. In: Meteorites: Flux with Time and Impact Effects; Grady, M.M., Hutchison, R., McCall, G.J.H., and Rothery, D.A., (Eds.), Geological Society of London, Special Publication 140, 133-152.

Koeberl C (2007) The geochemistry and cosmochemistry of impacts. In: Treatise of Geochemistry, Vol. 1 (ed. A. Davis), Elsevier, p. 1.28.1 -1.28.52, doi:10.1016/B978-008043751-4/00228-5.

Koeberl C, et al. (1997) Diamonds from the Popigai impact structure, Russia. Geology 25: 967-970.

Koeberl C (1990) The geochemistry of tektites, an overview. In: L.O. Nicolaysen and W.V. Reimold (Editors), Cryptoexplosions and Catastrophes in the Geological Record, with a Special Focus on the Vredefort Structure. Tectonophysics, 171: 405-422.

Koeberl C, Sigurdsson H (1992) Geochemistry of impact glasses from the K/T boundary in Haiti: Relation to smectites, and a new type of glass. Geochimica et Cosmochimica Acta 56, 2113- 2129.

Koeberl C, Brandstätter F, Hecht L, Reimold WU, Peck J, King J (2006) Uppermost Impact Fallout Layer in a Drillcore at the Bosumtwi Impact Crater (Ghana): A Preliminary Study. 37th Annual Lunar and Planetary Science Conference, March 13-17, 2006, League City, Texas, abstract no.1552.

Konyashin I, et al. (2006) A new hard allotropic form of carbon: Dream or reality? Int J Refract Met H 24:17–23.

Kurat G, Koeberl C, Presper T, Brandstätter F, Maurette M (1994) Petrology and geochemistry of Antarctic micrometeorites. Geochimica et Cosmochimica Acta, vol. 58, Issue 18, pp.3879-3904.

Kurbatov AV, et al. (2010) Discovery of Nanodiamond-rich Layer in Polar Ice Sheet (Greenland). Journal of Glaciology, v. 56, n 199, 749-759.

Kuznetsov VL, et al. (1994). Effect of explosion conditions on the structure of detonation soots: ultradisperse diamonds and onion carbon. Carbon, 32, 873–882

LeCompte MA, et al. (2011) Summary of unusual material in early Younger Dryas age sediments and their potential relevance to the YD Impact Hypothesis, paper presented at the XVIII INQUA Congress, held in Bern, Switzerland, July 21-27, 2011.

Lee MY, Chen C-H, Wei K-Y, Iizuka Y, Carey S. (2004) First Toba supereruption revival. Geology 32, 61–64.

Longinelli A, et. al., (2011) Delta 18O and Chemical composition of Libyan Desert Glass, country rocks, and sands: new considerations on target material. Meteoritics and Planetary Science: 46, No 2, 218-227.

Luetke S, Deutsch A, Berndt J, Langenhorst F (2008) Trace Elements in Ivory Coast Tektites, Microtektites, and Fallback Particles of the Lake Bosumtwi Impact Crater, Ghana: A LA-ICP-MS Study. 39th Lunar

and Planetary Science Conference, (Lunar and Planetary Science XXXIX), held March 10-14, 2008 in League City, Texas. LPI Contribution No. 1391., p.1613.

Maruyama K, Makino M, Kikukawa N, Shiraishi M (1992) Synthesis of hexagonal diamond in a hydrogen plasma jet. Journal of Materials Science Letters 11 (1992) 116-118.

Masaitis VL, *et al.* (1999) Impact diamonds in the Suevitic Breccias of the Black Member of the Onaping Formation, Sudbury Structure, Ontario, Canada. Large Meteorite Impacts and Planetary Evolution II, Proceedings of the International Conference held 1-3 September, 1997 in Sudbury, Ontario. Edited by B.O. Dressler and V.L. Sharpton. Boulder, CO: The Geological Society of America, p.317

Masaitis VL, *et al.* (1999) Impact diamonds in the Suevitic Breccias of the Black Member of the Onaping Formation, Sudbury Structure, Ontario, Canada. Large Meteorite Impacts and Planetary Evolution II, Proceedings of the International Conference held 1-3 September, 1997 in Sudbury, Ontario. Edited by B.O. Dressler and V.L. Sharpton. Boulder, CO: The Geological Society of America, p.317

Maurette M, Hammer C, Reeh N, Brownlee DE, Thomsen HH. (1986) Placers of cosmic dust in the blue ice lakes of Greenland. Science (ISSN 0036-8075), vol. 233, Aug. 22, 1986, p. 869-872.

McHugh CMG, Synder SW, Deconick J-F, Saito Y, Katz M, Aubry M-P (1996) Upper Eocene tektites of the New Jersey continental margin, Site 904. In: Mountain G. S., Miller K. G., Blum P., Poag C. W. and Twichell D. C. (eds). Proceedings of the Ocean Drilling Program, Scientific Results. United States Government Printing Office, Washington, D.C. USA. 150: 241-265.

McHugh CMG, Snyder SW, Miller KG. (1998) Upper Eocene ejecta of the New Jersey continental margin reveal dynamics of Chesapeake Bay impact. Earth and Planetary Science Letters. 160 (3-4): 353-367.

Metcalfe SE, Davies SJ, Braisby DJ, Leng JM, Newton JA, Terret LN,O´Hara LS (2007). Long and short term change in the Patzcuaro, basin. Paleogeography, Palaeoclimatology, Palaeoecology, 247, pp. 272-295.

Miller H, McIntire J, Southerland J (2001). Damage Controlman, NAVEDTRA 14057-PPR. Naval Education and Training Professional Development and Technology Center, NAVSUP Logistics Tracking Number 0504-LP-026-7250.

Misra S, *et al.* (2009) Geochemical identification of impactor for Lonar crater, India. Meteoritics & Planetary Science, vol. 44, Issue 7, p.1001-1018.

Orwa JO, *et al.* (2001) Diamond nanocrystals formed by direct implantation of fused silica with carbon. Journal of Applied Physics, Volume 90, Issue 6, pp. 3007-3018.

Povenmire H, Glass BP, Strange RL (1994) Discovery and description of a Muong Nong-type Georgia tektite. Abstracts of the Lunar and Planetary Science Conference. 25th: 1101-1102.

Povenmire H, Chance S (1997) Tektite from Jenkins County, Georgia. 28th Annual Lunar and Planetary Science Conference, March 17-21, 1997, Houston, TX, p. 1135.

Richard PJH, *et al.* (1997) Chronologie de la déglaciation en Gaspésie : nouvelles données et implications. Géographie physique et Quaternaire, vol. 51, n° 2, 1997, p. 163-184.

Rochette P (2008) Micrometeorites from the Transantarctic Mountains. PNAS November 25, 2008 vol. 105 no. 47 18206-18211.

Schmitt RT, Siebenschock M, Stöffler D (1999) Distribution of Impact Diamonds In The Ries Crater, Germany. Meteoritics & Planetary Science, vol. 34, Supplement, p.A102.

Schultz P (2004) The Quaternary impact record from the Pampas, Argentina. Earth and Planetary Science Letters 219 (2004) 221-238.

Scott AC, *et al.* (2010) Fungus, not comet or catastrophe, accounts for carbonaceous spherules in the Younger Dryas "impact layer." Geophysical Research Letters, Volume 37, Issue 14.

Smith PPK, Buseck PR (1981) Graphitic carbon in the Allende meteorite: a microstructural study, Science 212, 322-324.

Son TH, Koeberl C (2005) Chemical variation within fragments of Australasian tektites. Meteoritics & Planetary Science 40, Nr 6, 805–815.

Taylor S, Lever JH, Harvey RP (2000) Numbers, types, and compositions of an unbiased collection of cosmic spherules. Meteoritics & Planetary Science, vol. 35, no. 4, pp. 651-666.

Taylor S (2002) Micrometeorites from the South Pole water well. Boulder, CO, USA: National Snow and Ice Data Center. Digital media.

Tomita S, Fujii M, Hayashi S, Yamamoto K (2000) Transformation of carbon onions to diamond by low-temperature heat treatment in air. Diamond and Related Materials, Vol. 9, pp. 856-860.

Trnka M, Houzar S (2002) Moldavites: a review. Bulletin of the Czech Geological Survey, Vol. 77, No. 4, 283–302.

Valter AA, Gurskij DS, Erjomenko GK (2000) Distribution of Impact Diamond in the Belilovka (Zapadnaja) Astrobleme on Ukrainian Shield. 31st Annual Lunar and Planetary Science Conference, March 13-17, Houston, Texas, abstract no. 1215.

Weninger, B, Joris, O, Danzeglocke, U (2007) CalPal-2007: Cologne Radiocarbon Calibration and Palaeoclimate Research Package (Cologne University, Cologne, Germany) (http://www.calpal.de).

Wolbach WS, Lewis RS, Anders E. (1985) Cretaceous extinctions: evidence for wildfires and search for meteoritic impact. Science 230: 167-170.Wolbach WS (1990) Carbon across the Cretaceous-Tertiary Boundary, Ph.D. Thesis, the University of Chicago.

Wolbach WS, Gilmour I, Anders E (1990) Major wildfires at the Cretaceous/Tertiary boundary, in Sharpton, V.L., and Ward, P.D., eds., Global catastrophes in Earth history: Geological Society of America Special Paper 247, p. 391–400.

Yastrebov S, Smith R (2009) Nanodiamonds enveloped in glassy carbon shells and the origin of the 2175 Å optical extinction feature. The Astrophysical Journal, 697:1822–1826.

Yoshimoto MK, *et al.* (1999) Epitaxial diamond growth on sapphire in an oxidizing environment. Nature 399, 340-342.

Zarate-del-Valle PF, Ramırez-Sanchez HU, Fernex F, Simoneit BRT, Israde-Alcantara I (2009) Radiocarbon age inversions and progression: source and causes in Late Holocene sediments from Lake Chapala, western Mexico. Environ Earth Sci.

Zolensky ME, Koeberl C. (1991) Why are blue zhamanshinites blue? Liquid immiscibility in an impact melt. Geochimica et Cosmochimica Acta (ISSN 0016-7037), vol. 55, May 1991, p. 1483-1486.